Laser-Induced Particle Impact Testing in High-Pressure Oxygen Environments

by

Samair Alyassini

B.S. Aerospace Engineering
Texas A&M University, 2016

Submitted to the Department of Mechanical Engineering in
partial fulfillment of the requirements for the degree of

MASTER OF SCIENCE IN MECHANICAL ENGINEERING

at the

MASSACHUSETTS INSTITUTE OF TECHNOLOGY

June 2023

Signature of Author: _____
Samair Alyassini
Department of Mechanical Engineering
May 23, 2023

Certified by: _____
Zachary Cordero
Department of Aeronautics and Astronautics
Thesis Supervisor

Certified by: _____
Douglas Hart
Department of Mechanical Engineering
Department Reader

Accepted by: _____
Nicolas Hadjiconstantinou
Chairman, Department Committee on Graduate Thesis

Laser-Induced Particle Impact Testing in High-Pressure Oxygen Environments

by

Samair Alyassini

Submitted to the Department of Mechanical Engineering
on May 23, 2023, in partial fulfillment of the
requirements for the degree of
Master of Science in Mechanical Engineering

Abstract

Particle impact ignition is an important source of metal fires in the high-pressure oxygen environments found in the turbines of oxygen-rich turbopumps. Understanding of particle impact ignition has been hindered by experimental challenges in reproducing this phenomenon under controlled laboratory conditions. This study addresses these challenges through the development of a specialized particle impact rig that integrates laser-induced particle impact testing (LIPIT) into an oxygen-compatible pressure vessel, thus enabling precise control over environmental conditions (target temperature, oxygen pressure) as well as impact variables (particle size/shape, impact velocity). This thesis describes the design of the oxygen-compatible pressure vessel, emphasizing considerations such as stress analysis, materials selection, oxygen-compatibility, and integration with the LIPIT system. The thesis concludes with pathfinding experiments successfully demonstrating particle ignition in a prototype rig, providing in situ images of single particle ignition events using application-relevant materials and particle sizes. Future work will use this rig to characterize the effects of operating conditions and material choices on susceptibility to particle impact ignition with a view toward developing more durable oxygen-compatible hardware for next-generation staged combustion rocket engines.

Thesis Supervisor: Zachary Cordero
Title: Assistant Professor
Thesis Reader: Douglas Hart
Title: Professor

Acknowledgments

As I approach the culmination of my MIT graduate school journey, I am overwhelmed with a deep appreciation for the remarkable individuals who have played an instrumental role in transforming my aspirations into tangible achievements. Chief among them, my advisor, Zack Cordero, shines brightly as a beacon of unwavering support, invaluable mentorship, and unparalleled guidance. In moments of difficulty and uncertainty, Zack's steadfast belief in my abilities has propelled me forward, offering guidance and steering me back on track.

My heartfelt gratitude also extends to the exceptional particle ignition research team, including Spencer Taylor, and Drs. Steve Kooi and Suhas Eswarappa Prameela. Their invaluable contributions and collaborative spirit have been pivotal to the success of this thesis. I am particularly grateful to Spencer for his tireless dedication, spending long hours in the lab collecting the vital validation data crucial for the completion of this research. Expressing the true depth of my gratitude may prove challenging, but I will forever cherish and be thankful for his immense contributions.

Finally, I want to express my heartfelt appreciation to my wife for her unwavering support and understanding throughout the course of my master's program. Her love and encouragement have been a constant source of strength and motivation, and I am deeply grateful for her presence in my life.

The completion of my master's degree stands as an extraordinary milestone, one that I once believed to be beyond my grasp. Looking back, I am humbled by the profound personal and academic growth I have experienced during this transformative journey. I profoundly appreciate those who have supported and guided me along the path.
WWNF

Table of Contents

List of Figures

List of Tables

CHAPTER 1: Introduction

1.1 Background

The development of reusable rocket engines presents a set of challenges distinct from those encountered in conventional expendable rocket engines [1]. These challenges arise from such factors as rapid thermal transients, extreme thermal gradients, high heat fluxes, and high-pressure oxygen environments, which push materials to their physical limits and give rise to potentially catastrophic failure modes. The thrust chamber, turbopump, and nozzle are the three critical components that limit the service life of a reusable rocket engine. Each component operates under unique conditions, experiences different failure modes, and requires careful consideration of materials selection. Oxygen-rich turbopumps, for instance, can fail via metal fires that result from frictional ignition or particle impact ignition, necessitating the use of specialized oxygen-compatible materials and coatings. Currently, high-strength superalloys are often used as rotors in oxygen-rich turbopumps despite their flammability, underscoring the need for a deeper understanding of the underlying ignition phenomena and the development of new ignition-resistant materials [1].

In high-pressure oxygen-rich environments, foreign/domestic object debris (FOD/DOD) impacting other components represents a concern in terms of ignition mechanisms. FOD/DOD particles in oxygen-rich chambers are accelerated to flow path velocities. As the flow path changes direction, these particles can impact surfaces, resulting in particle ignition due to the transfer of kinetic energy. The ignition of the particle acts as kindling, and the ignition process propagates to the impacted component. The oxidizer-rich preburner and turbine in oxygen-rich staged combustion and full-flow staged combustion rocket engines operate under pressures of several ksi of oxygen [1]. This high oxygen pressure increases the risk of metal ignition. To mitigate this risk effectively, the characterization of particle impact ignition of metallic alloys under representative operating conditions is needed to gain a deeper understanding of this ignition mechanism to ensure the safety and reliability of rocket engines.

During development of the space shuttle main engine, NASA White Sands Test Facility (WSTF) conducted experiments to rank and characterize the ignition behavior of metals in high-pressure gaseous oxygen. WSTF tested multiple metals under fixed conditions and published the results [2] providing the foundation for selecting materials suitable for oxygen-rich environments. However, advancements in alloys, manufacturing techniques, and particle impact testing methods have been made since then.

Particle impact ignition tests have historically involved directing a stream of gaseous oxygen, carrying one or more particles, onto a test sample [2]. These tests can be conducted in either supersonic or subsonic conditions, with experimental variables including oxygen pressure,

temperature, velocity, and particle characteristics. In supersonic tests, the gas temperature can reach 800°F, and particle velocity and pressure at the target increase gradually with the target temperature. Subsonic tests, on the other hand, allow for variations in gas velocity by using different orifice sizes. Temperature effects are influenced by factors such as particle size and ease of oxidation, typically resulting in increased ignitability with higher temperatures, but oxidation at elevated temperatures can reduce it.

The main objective of this thesis was to introduce a novel tool for investigating particle impact ignition in a controlled, high-pressure oxygen-rich environment. The focus was on enabling the observation of particle impact and ignition events in real time, ensuring safety while operating within a wide range of pressures and particle velocities.

1.2 Laser-Induced Particle Impact Testing

Laser-Induced Particle Impact Testing (LIPIT) is a recently developed technique for launching particles at targets under controlled conditions [1]. It is especially well-suited for studying particle impact ignition as its capabilities align well with the combinations of particle size and speed commonly encountered in applications (**Figure 1.1**). Another important advantage of LIPIT is it can be fitted with in situ imaging capabilities which offer microscale spatial resolution and nanosecond temporal resolution, potentially enabling direct observations of particle burning. LIPIT has been successfully used to study particle adhesion for cold spray applications [2], ballistics and erosion [3], as well as aerospace textiles development testing [4].

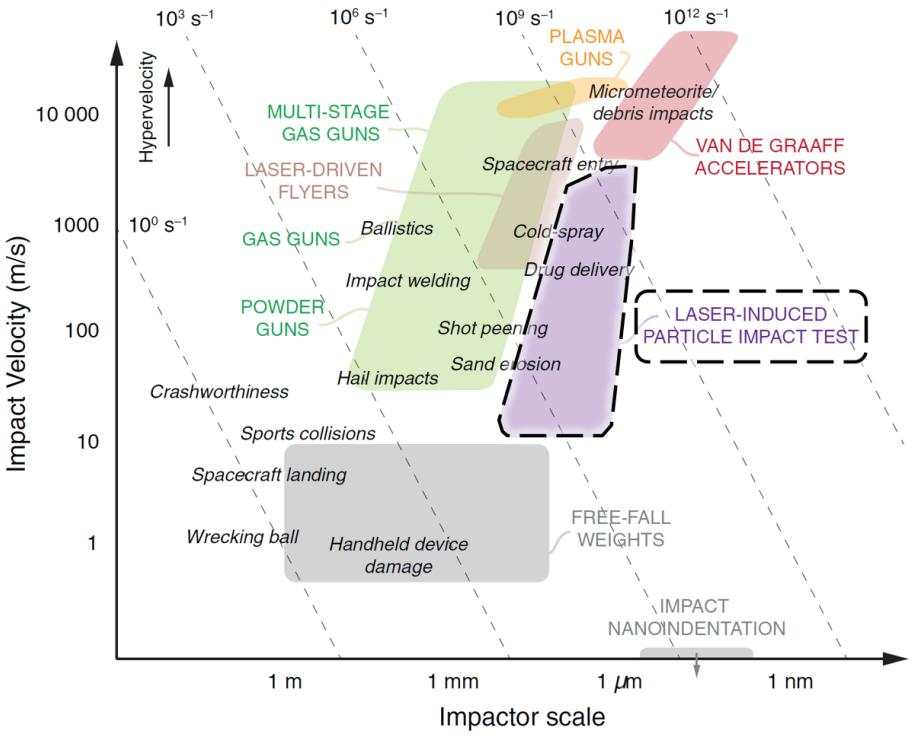

Figure 1.1: Particle impact testing methods capability (Taken from [1])

LIPIT uses a high-power laser to ablate material on a launch pad to launch a particle with controlled velocity towards a target (**Figure 1.2**). The particle location can be independently controlled by the user to get the particle in the focus of the optics system, which ensures the alignment of the laser to the particle. The target position may also be adjusted to manipulate the point of impact on the target surface.

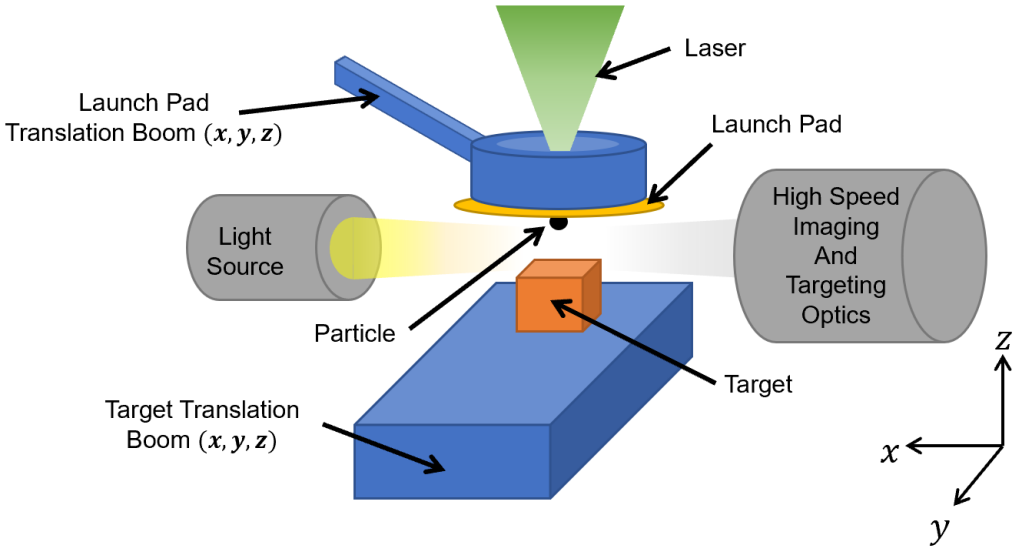

Figure 1.2: Diagram of LIPIT apparatus

A key component of LIPIT is the launch pad, which consists of a glass substrate, an ablation layer (typically gold), and an elastomer layer with particles on the surface. The LIPIT Nd:Yag laser system is to create a localized heat, which in turn ablates the gold creating a plasma. The plasma the rapidly deforms the elastomer layer, accelerating the particle (**Figure 1.3**).

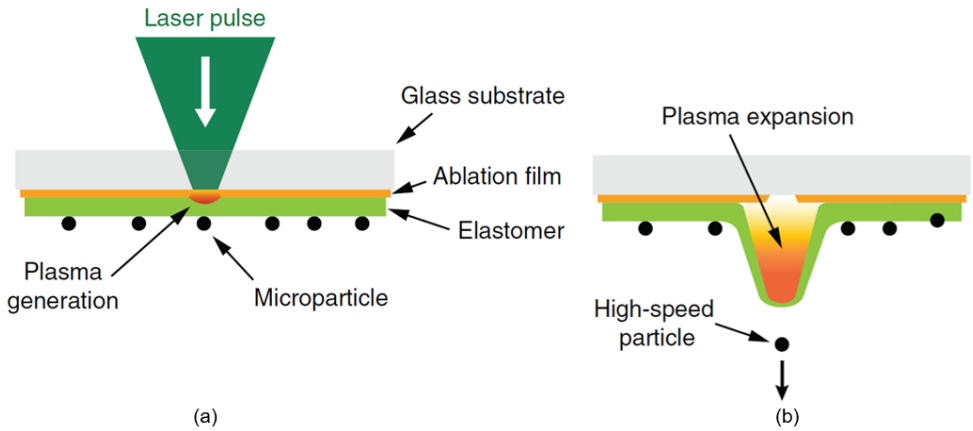

Figure 1.3: LIPIT launch pad (Taken from [1]). (a) shows the laser hitting just above a particle and (b) is immediately after the laser is fired the plasma expansion launches the particle at high speed.

The target specimen sits approximately 0.020 inches directly below the particle. High-speed microscopy captures the particle and a multi-frame image is generated. **Figure 1.4** shows time-series images from a LIPIT experiment in which an Al particle impacts then adheres to a rigid target.

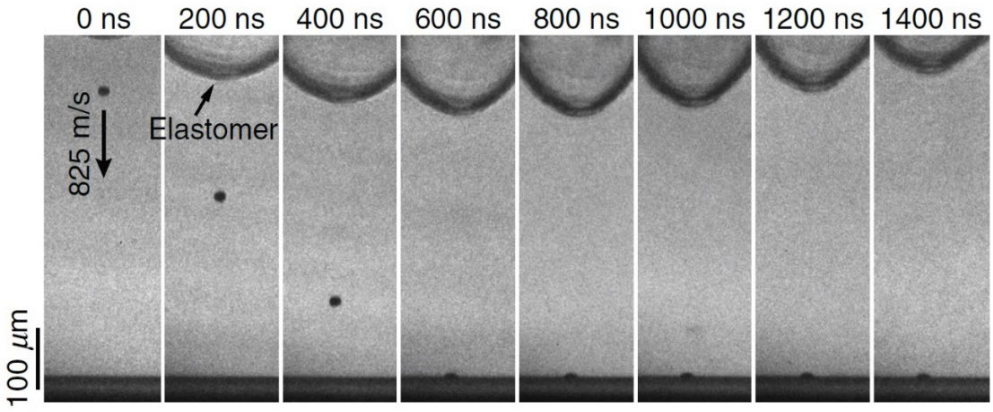

Figure 1.4: Example of LIPIT in situ images (Taken from [1])

LIPIT is an attractive approach for studying particle impact ignition in high-pressure oxygen environments, as it eliminates the need for mechanical feedthroughs into the pressure vessel. The

only requirement is that the laser and high-speed microscopy systems can optically access the launch pad, which can be incorporated into the pressure vessel.

1.3 Oxygen Compatibility

Oxygen compatibility and resistance to metal fires are critical considerations in the design and safe operation of a high-pressure oxygen system. The ignition temperature of a metal is influenced by factors such as the test method, material configuration, and the presence of oxide layers. Typically, the ignition temperature of a metal is equal to or higher than its melting point, and the flame temperature is equal to or higher than the boiling point or decomposition temperature of the metal oxide. While ceramics and glasses are not commonly used in oxygen systems, they are considered inert [5].

Metal ignition is an extremely exothermic reaction, greatly increasing the probability of surrounding materials within the pressure vessel test chamber coming into contact with burning metal spatter. One strategy leveraged from high-pressure promoted metal ignition testing is the use of protective and sacrificial components.

Lastly, rapid pressurization of the oxygen system requires prevents the use of long flexible, non-metallic, hose and tubing. Rapid pressurization can cause adiabatic heating over the autoignition point of commonly used flexible hose and tube materials such as Teflon and Vespel [5], The use of distance volume pieces can be used to mitigate the risk of igniting such materials [6].

1.4 Thesis Outline

The main objectives of this thesis are the development and successful implementation of an oxygen-rich pressure vessel compatible with the LIPIT system. The key design considerations include operator safety, ease of use, oxygen compatibility, reusability, and compatibility with LIPIT optics. A prototype pressure vessel is used in pathfinding high-pressure oxygen LIPIT experiments to demonstrate particle ignition.

This thesis is organized as follows:

- Chapter 2 summarizes the design requirements and design features.
- Chapter 3 outlines the analysis method and results used in the design of the pressure vessel including finite element analysis modeling.

- Chapter 4 presents preliminary observations of particle impact ignition testing in high pressure oxygen, collected using a prototype high-pressure oxygen LIPIT system.
- Chapter 5 summarizes the key findings and future work associated with the outcomes in this thesis.

CHAPTER 2: Overview of HiPO LIPIT

2.1 Design Requirements

The primary objective of the High-Pressure Oxygen Laser-Induced Particle Impact Test (HiPO LIPIT) system is to collect data regarding particle impact ignition, such as burn time and impact characteristics, for various particle/target combinations. This chapter describes the design of a test chamber with a maximum working pressure of 2.5 ksi that is constructed with oxygen-compatible materials, is consistent with industry-standard design criteria for safe pressure vessels (e.g., ASTM Manual 36 [5], ASME Boiler and Pressure Vessel Code [7]), and integrates with a LIPIT system at the MIT Institute for Soldier Nanotechnologies (ISN).

The LIPIT system incorporates optics and laser systems with specific focal distance requirements:

- The distance between the particle and the imaging objective lens must be less than 3.25 inches to image the micron-sized particles.
- The laser focal point must be less than 3 inches to ensure the appropriate laser spot size at the launch pad.
- The windows must be sufficiently large to allow for the relative motion between the laser and particle during the test.

2.2 Design Overview

The HiPO LIPIT Pressure Vessel design, developed through a series of iterations over the course of this thesis, is shown in **Figures 2.1** and **2.2**. The rig consists of four sub-assemblies: the pressure vessel, the gas pressurization control system, a 3-axis translational alignment system and the specimen fixturing device. All materials were selected using ANSYS Granta EduPak software [8] and ASTM Manual 36 [5] to optimize strength and oxygen compatibility. The test chamber volume was intentionally kept small to minimize material usage and improve safety. The test specimens are inserted into the fixturing device and then placed inside the test chamber. The pressure vessel cap used to enclose the pressure also holds the test samples in place. Once the cap is secured in place using the clamp, the vessel can be pressurized using a high-pressure oxygen gas cylinder and pressure regulator. A network of tubing, gauges, and valves allows the user to pressurize and vent the test chamber. The X, Y, and Z directional translational stages are used to align the particle with the laser and execute the test.

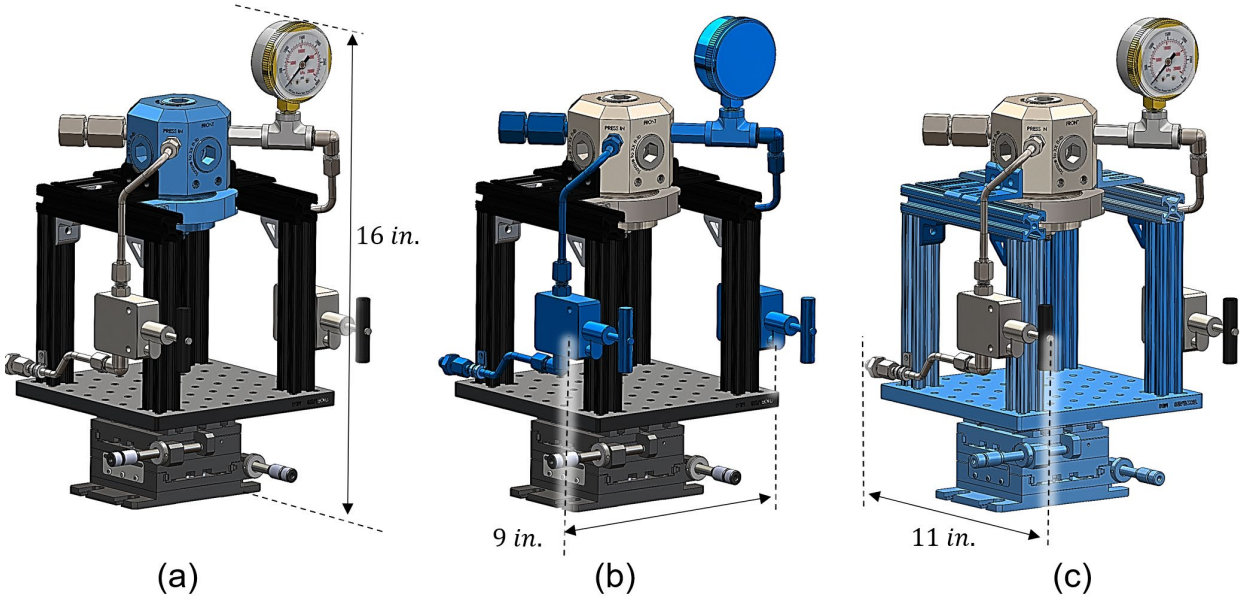

Figure 2.1: Images of the HiPO LIPIT major sub-assemblies. The (a) pressure vessel, (b) pressurization control system, and (c) 3-axis translational alignment system are individually highlighted

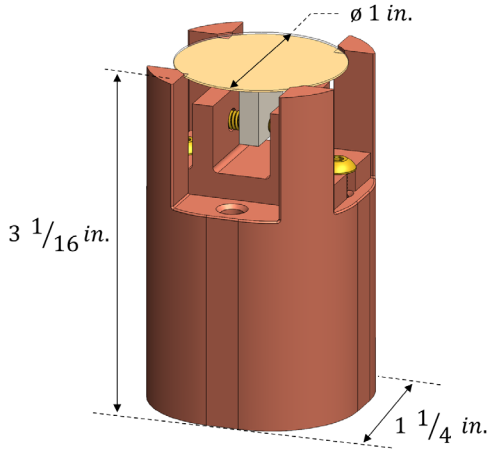

Figure 2.2: Image of specimen fixture sub-assembly

2.2.1 Specimen Fixture Sub-Assembly

The specimen fixture sub-assembly is composed of copper and brass, selected for high ignition-resistance [5]. It features a four-pedestal base to support the launch pad and four threaded-through holes to mount the holder using two screws **(Figure 2.3)**. The holder and base were intentionally designed as two pieces to enable future modifications to support alternative launch pad and target form factors.

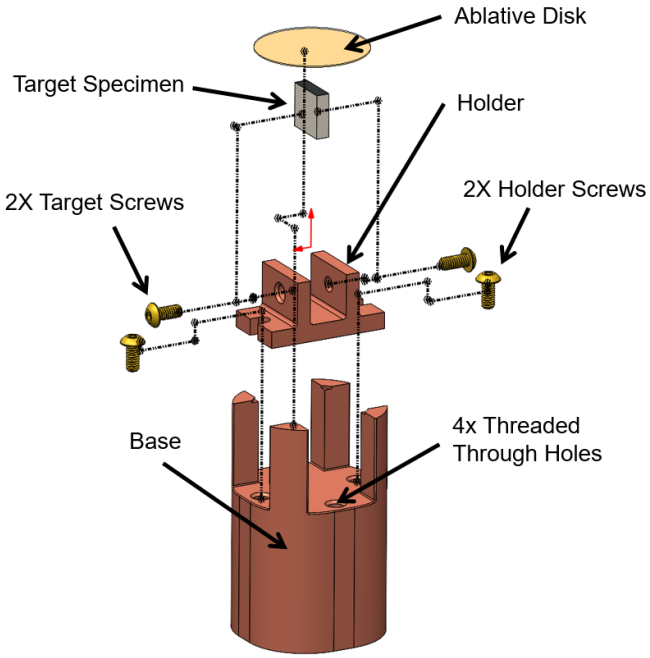

Figure 2.3: Exploded view of specimen fixture sub-assembly

2.2.2 Pressure Vessel Sub-Assembly

The pressure vessel sub-assembly comprises a main body with five window ports and a cap. The V-band coupling fastens the cap to the pressure vessel, providing a secure high-strength seal. The load-bearing windows are secured using mechanical retention via window retaining screws and O-ring seals. The pressure vessel body includes four provisions for gas services, including a supply, vent, exhaust, and a spare port for future use, shown in **Figure 2.5**. The pressure vessel has a maximum working pressure (MWP) of 2.5 ksi and a proof pressure criterion of twice the MWP (5 ksi) to prevent permanent damage to the vessel due to inadvertent overpressure. A conservative analysis considering the proof pressure is given in **Chapter 3**.

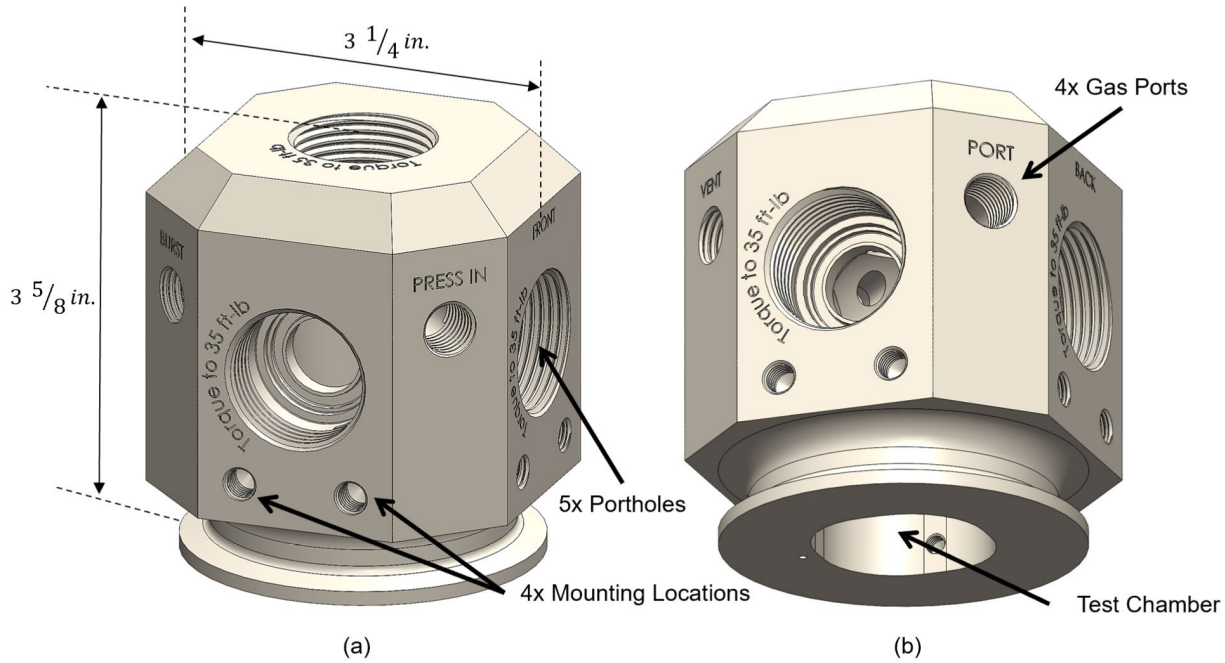

Figure 2.4: Pressure vessel body features shown on the (a) right and (b) left sides

Figure 2.5 shows the components and layout of the pressure vessel sub-assembly. Both the pressure vessel and cap are made from work-hardened Monel 400 due to its strength and ignition-resistance [5]. The load-bearing windows are 1-inch diameter and 0.196-inches thick, and made of sapphire (Al_2O_3). A second protective sapphire window 0.040 inches thick is used to protect the load-bearing windows from ignition debris. Sapphire was chosen due to its high modulus of rupture, as well as high transmission in the visible (0.4-0.7 μm) and near-infrared (0.8-2.5 μm) spectra [9]. The window retention screws are made from AISI 304, ¼ hard stainless steel for strength [8]. The threads of the window retention screw are silver-coated to avoid galling and improve lubricity during torquing. All O-ring seals are made from Viton for oxygen compatibility [5] and seal glands sized in accordance with industry standards [10]. The chamber walls are lined with a 0.125-inch-thick copper insert to protect the chamber from spatter from metal fires. The clamps are made from A-286 superalloy steel for high strength, similar design to a typical aerospace grade coupling [11].

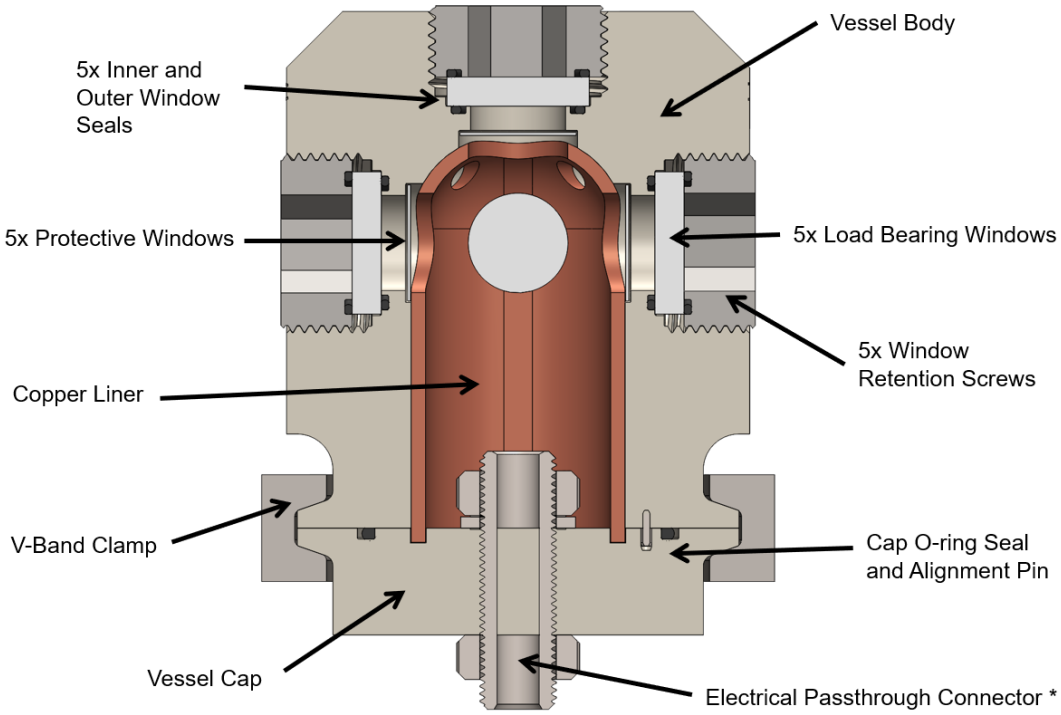

Figure 2.5: Cross sectional view of pressure vessel sub-assembly
**The Electrical Passthrough Connector is not a design requirement but is used as a place holder for future HiPO LIPIT system upgrade*

2.2.3 Gas pressurization control system

The gas pressurization control system is shown in **Figure 2.6** while the flow path is summarized in **Figure 2.7**. The control system comprises 316 stainless steel and brass, selected for their oxidation and ignition resistance [5]. Regulated oxygen pressure is supplied to the pressure valve through supply tubing from a high-pressure gas cylinder [12]. The chamber pressure is controlled manually using the slow opening pressure and exhaust valves to prevent rapid compression. To prevent damage in case of accidental overpressure, a 3 ksi rupture disk is used to rapidly de-pressurize the test chamber if it exceeds 120% of the MWP. Brass sinter filters are installed at all gas ports to prevent any burning material from entering the pressurization system as a safety precaution in case of rapid decompression.

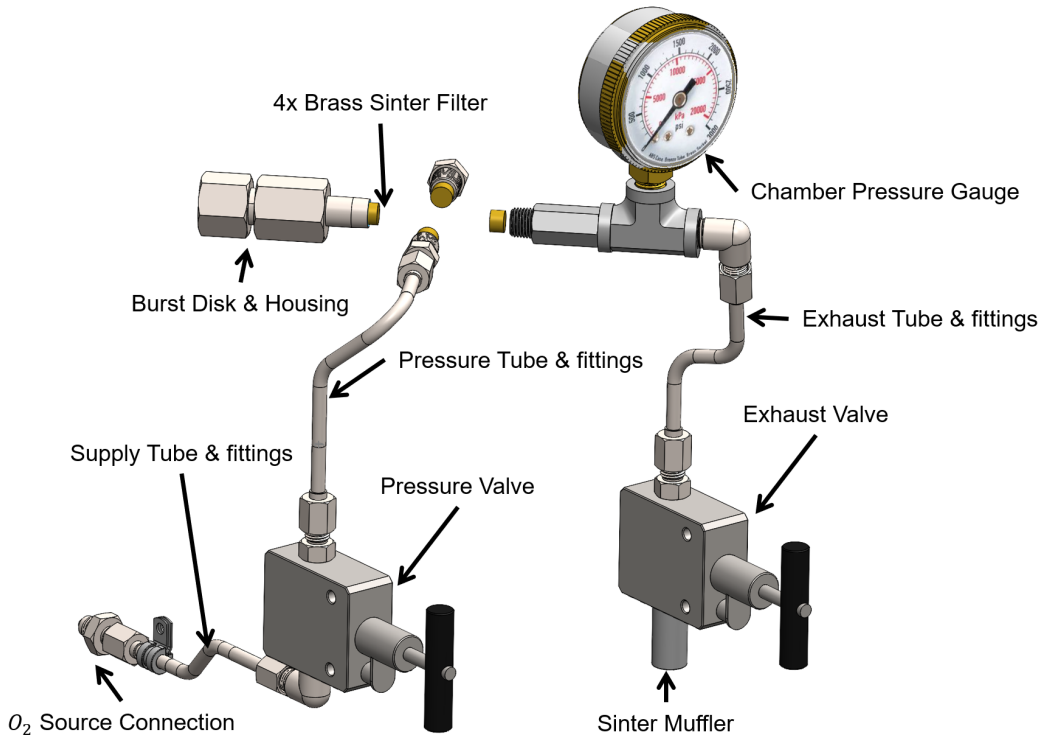

Figure 2.6: Gas pressurization control system

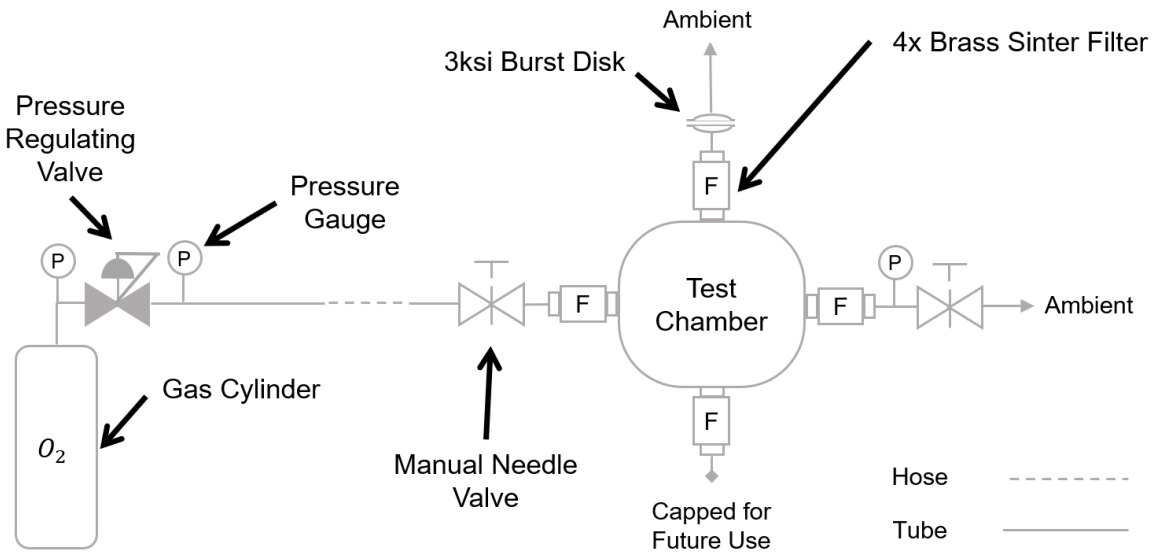

Figure 2.7: Flow diagram of gas pressurization control system

The gas pressurization control system will mainly consist of off-the-shelf fittings, tubing, housings, gauges, filters, and valves. All tubes and fittings are certified to withstand a MWP of 3 ksi which exceeds the MWP of the pressure vessel.

2.2.4 3-Axis Translational Alignment System

The 3-axis translational alignment system is designed with an aluminum 80/20 extruded frame section supported by gussets, an 8×8-inch breadboard, and a 3-axis transitional stage assembly, along with attachment hardware seen in **Figure 2.8**. The system includes a raised platform, which provides a convenient 6-in³ workspace centered underneath the pressure vessel sub-assembly for loading and unloading of specimens. The frame sections are also equipped with mount locations for the gas pressurization control system valves and tube clamps, ensuring optimal placement and easy access.

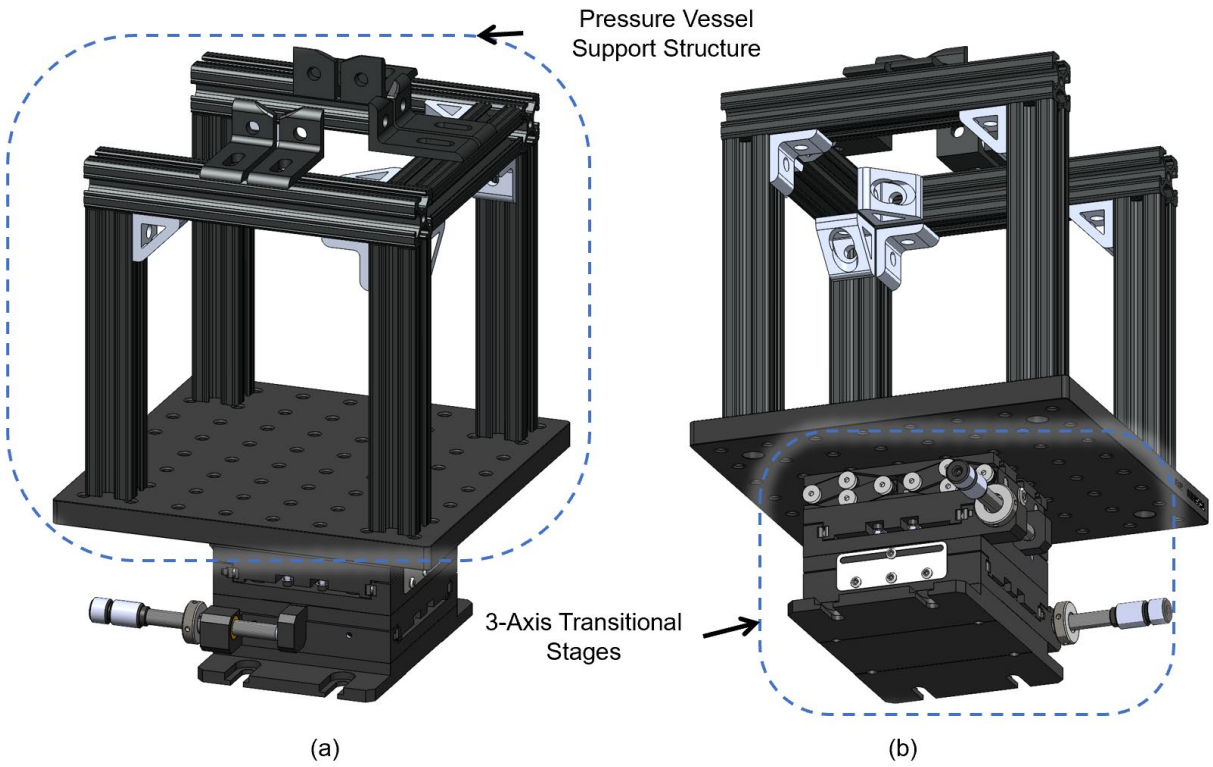

Figure 2.8: 3-Axis translational alignment system shown on the (a) right and (b) left sides

CHAPTER 3: Stress, Safety, and Lifing Analysis

This chapter presents an analysis of stress-induced failure modes and assessments of pressure vessel safety under realistic operating conditions. The analysis proceeds along two complementary steps. The initial step is a first-order stress assessment, focusing on preliminary sizing considerations such as the constraints on optical distance summarized in **Section 2.1**. This assessment provides an initial understanding of the stress distribution and establishes a baseline for further analysis. Following preliminary sizing, a more detailed finite element analysis (FEA) is conducted, enabling identification of specific stress concentrations, interactions, and potential failure points within the pressure vessel. The stress analysis ensures pressure vessel integrity, considering fatigue of each component as well as adiabatic heating resulting from the rapid compression of the oxygen supply system.

3.1 ASME BPVC Stress Analysis

Preliminary sizing of the pressure vessel thickness was accomplished using ASME BPVC [7], an industry-standard methodology for pressure vessel design. The main outputs from these calculations are the stress (S_T) at the three key locations of the vessel identified in **Figure 3.1**; locations of primary interest are the side mid-wall (A, D), intersection of wall and corner radius (C, B), and the corner of the vessel. To satisfy the code and ensure safe operation [7], S_T must always be less than the room-temperature yield strength of Monel (16.7 ksi).

The vessel design has four-fold symmetry about the particle travel direction **(Figure 3.1)**. Therefore, the side mid-wall lengths (L) are equal , and the wall thickness (t) is uniform about the radius. Total stress at the mid wall (A, D) is the sum of local membrane stress S_m and bending stress S_b:

$$S_{T_A} = S_{T_D} = S_{m_{A,D}} + S_{b_{A,D}}. \quad \textbf{(1)}$$

Similarly, total stress at the side wall adjacent to the corner (points B and C) is

$$S_{T_B} = S_{T_C} = S_{m_{B,C}} + S_{b_{B,C}}. \quad \textbf{(2)}$$

For the corner sections (point B to C), the total stress is calculated using

$$S_{T_{B\to C}} = S_{m_{B\to C}} + S_{b_{B\to C}}. \quad \textbf{(3)}$$

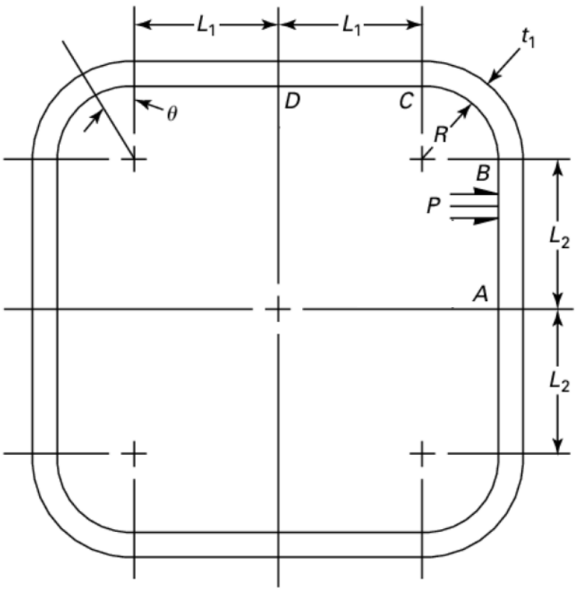

Figure 3.1: Diagram of pressure vessel with a rectangular cross section (Taken from [7])

The membrane stresses at wall locations are calculated using

$$S_{m_A} = S_{m_B} = S_{m_C} = S_{m_D} = \frac{P(L+R)}{t}, \tag{4}$$

while the membrane stresses at the corner B to C are calculated using

$$S_{m_{B\to C}} = \frac{P(2L+R)}{t}. \tag{5}$$

Bending stresses at wall locations are calculated using

$$S_{b_A} = S_{b_B} = S_{b_C} = S_{b_D} = \frac{tb}{4I}(2M + PL^2), \tag{6}$$

while the bending stresses at the corner are calculated using

$$S_{b_{B\to C,max}} = \frac{t}{4I}(2Mb + 2PRL^2), \tag{7}$$

and area monent of inertia I of a rectangular section is defined as

$$I = \frac{bt^3}{12}. \tag{8}$$

This bending stress calculation assumes a unit length (b=1in. for out of plane vessel width moments) so that M has units of in-lb/in. The shape factor (K) for an unreinforced rectangular vessel is given as 0.11 in² [7]. The bending unit moments M is

$$M = PK, \tag{9}$$

These expressions were used to establish the minimum required dimensions of thickness (0.385 inches), total wall length (0.2 inches), and corner radius (0.5 inches) which satisfy the stress threshold of 16.7 ksi under a worst-case internal pressure of 5 ksi.

The final design dimensions of wall thickness (0.552 inches), total wall length (0.2 inches), and corner radius (0.65 inches) resulted in the maximum stress location to be the corner bending stress, $S_{T_{B\to C}}$ of 12.2 ksi. This stress value represents a 27% margin of safety below the already conversative stress threshold requirement. Peak stresses at the mid wall and side wall adjacent to the corner locations were $S_{T_A} = S_{T_D} = 8.7$ ksi and $S_{T_B} = S_{T_C} = 9.2$ ksi, respectively.

3.2. Stress Concentrations

Peterson's Stress Concentration Factors [13] are used to estimate the peak localized stress the top and side of the pressure vessel portholes. The present assessment assumed the geometry of single circular hole in an infinite thin element under biaxial stress, as shown in **Figure 3.2**. The stress concentration factor for the top (location A) of the hole is

$$K_{t,A} = 3\frac{\sigma_2}{\sigma_1} - 1. \quad \textbf{(10)}$$

The stress concentration factor for the side (location B) of the hole is defined by

$$K_{t,B} = 3 - \frac{\sigma_2}{\sigma_1}. \quad \textbf{(11)}$$

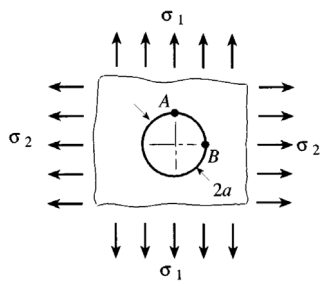

Figure 3.2: An infinite thin element under biaxial tensile in plane loading (Taken from [13])

The multipliers were calculated to be $K_{t,A} = 3.21$ and $K_{t,B} = 1.6$ using the mid-wall stress as the vertical stress ($\sigma_1 = S_{T_D} = S_{T_A}$) and corner stresses as the horizontal stress ($\sigma_2 = S_{T_{B\to C}}$). Applying these concentration factors to the to the respective locations around the porthole resulted in 27.9 ksi at location A and 19.5 ksi at location B . This estimate for peak concentrated stress is 27.6% of the 0.2% yield strength of the Monel material used.

3.3 Window Retention Sizing and Stress

Crystran LTD [14] has published equations to size high-pressure windows based on geometry and loading. **Figure 3.3** graphically depicts the HiPO LIPIT window. The minimum allowable window thickness for a clamped window is

$$t = D\sqrt{\frac{P \times SF \times K}{4M_r}}, \tag{12}$$

where the pressure load P differential, material rupture modulus M_R, safety factor SF, unsupported diameter D, and clamp effect factor $K = 0.75$. The recommended minimum safety factor is 4 for pressure differential greater than 1 atmosphere.

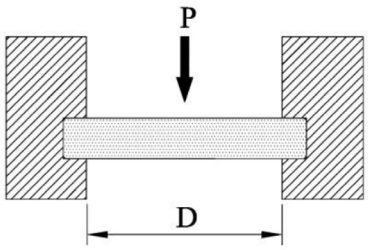

Figure 3.3: Diagram of circular window geometry and loading (Taken from [18])

A window retaining screw is used to support the window and to facilitate rapid assembly and replacement. To determine the required value in which to torque the window screw, an understanding of the loads that it must support needs to be calculated. The load the window screw needs to support is determined by

$$F_{rxn} = P_{proof} \times A_{window}, \tag{13}$$

where the reaction load (F) is the product of the pressure (P) acting on the surface (A) of the window. For threaded screw couples, the torque-to-clamp load of a threaded screw is not a 1:1 relationship primarily due to friction. Using [15] determines the torque (T) of the window screw for a given thread pitch diameter (D) and accounting for the material couple factor (K), and the friction effect due to lubrication (L). Torque of the window is calculated using

$$T = F_{rxn} \times D_{screw} \times K \times (1 - L), \tag{14}$$

where $K = 0.15$ and L=40% [16], and the thread pitch diameter D of 1.25 inches.

The thread stress concentration factor of standard a v-thread is approximately 2.8 [13]. Combining these concentration factor to the screw stress yields

$$\sigma_{thread} = K_t\, \sigma_{screw} = K_t \frac{F_{rxn}}{A_s}, \quad \textbf{(15)}$$

where A_s is the total threaded contact area. This equation is used for estimating the peak stress in the root of the v-thread.

A 1-inch diameter, 0.196-inch-thick sapphire window was selected to satisfy the constraints on optical access. According to **equation (12)**, this combination of window size and material gives a safety factor of 5.8. The minimum required window retention screw torque is 34.75 ft-lbs, giving a thread stress of 48.4 ksi using **equations (14)** and **(15)**, respectively.

3.4 FEA Models

To ensure all possible load combinations and limiting stress locations were identified, four ANSYS Workbench™ finite element analysis (FEA) models were created. These models included: a full 3D pressure vessel model, a 3D pressure vessel wedge model, a 3D v-band clamp model, and a 2D axisymmetric window retention screw model. Isotropic material properties were imported from ANSYS Granta EduPak software [8] and assigned to the relevant bodies in the FEA models. Models that simulated sliding/friction contacts used average friction values [17] of specific material couples to capture the shearing effects. SOLIDWORKS® CAD files were converted to parasolid (.x_t extension) files and imported into Workbench™. All analyses use quadratic nodes/elements, are linear-elastic, and assume room temperature.

3.4.1 3D Pressure Vessel Model

The 3D pressure vessel model is shown in **Figure 3.4**, which highlights the mesh quality, including nodes/elements, element type, and material for each component. **Figure 3.5** displays the boundary conditions (loads and displacements) of the 3D pressure vessel model. This model prioritizes efficiency and rapid iteration of designs, focusing on overall performance rather than modeling all design details. By excluding small features, the analysis is more computationally efficient, allowing for faster iterations. However, this approach did not capture all localized stress concentrations. The model was sufficient for assessing bulk body stresses and understanding global behavior.

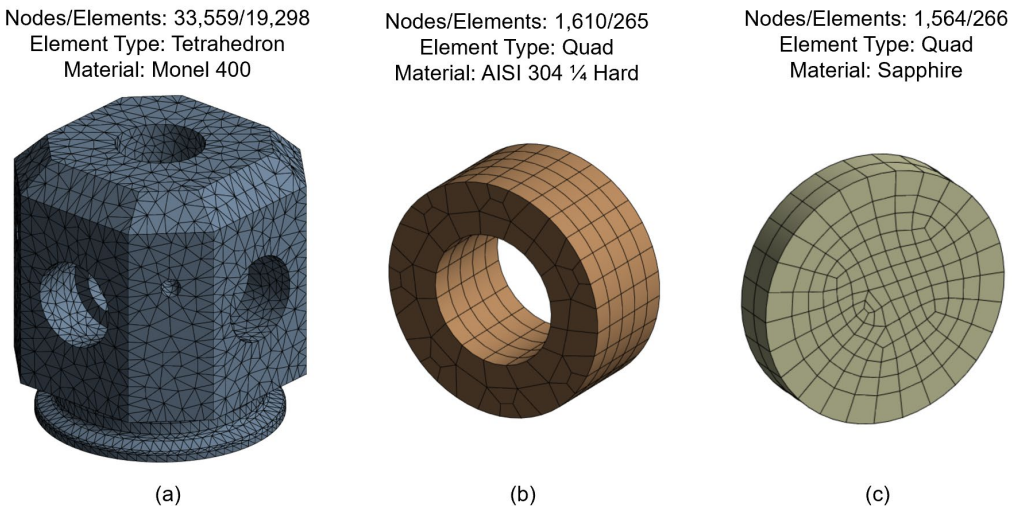

Figure 3.4: 3D Pressure vessel model mesh details of the (a) pressure vessel body (b) window retention screw, and (c) window

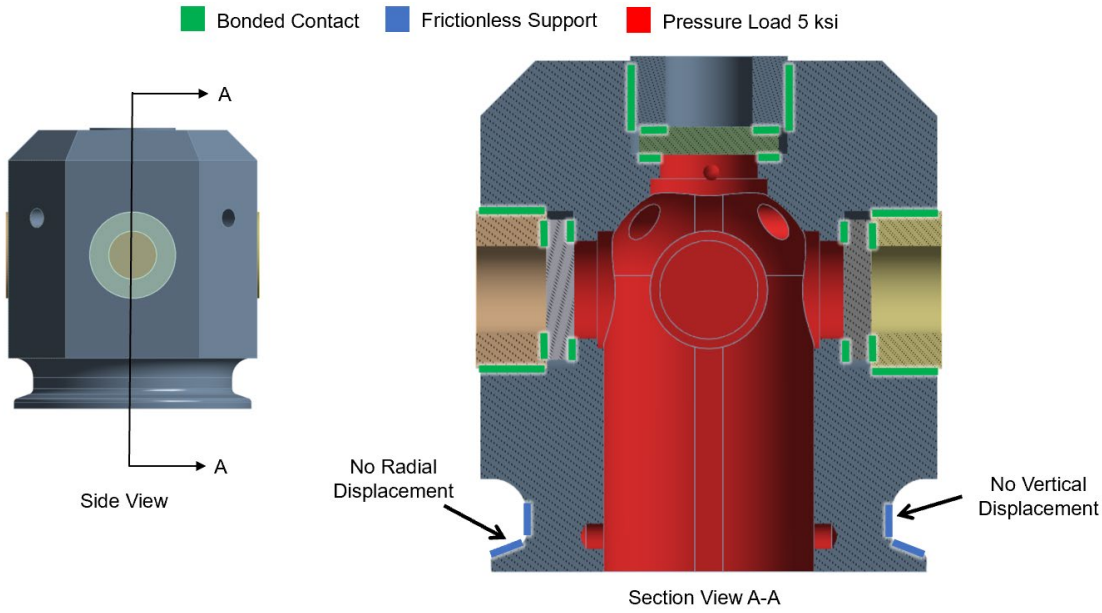

Figure 3.5: View of 3D pressure vessel model boundary conditions

Stress and displacement results are summarized in **Figure 3.6** which compare well with the baseline calculations stresses. Pressure vessel side wall and corner stresses resulted in 9 ksi and 12 ksi, respectively, and were slightly less (0.2 ksi) than the stresses assessed in **Section 3.1**. The peak stress of 24.7 ksi located in the bottom of the window was 3.2 ksi less than the predicted concentrated stress assessment in **Section 3.2** and is 25% of the yield strength of Monel.

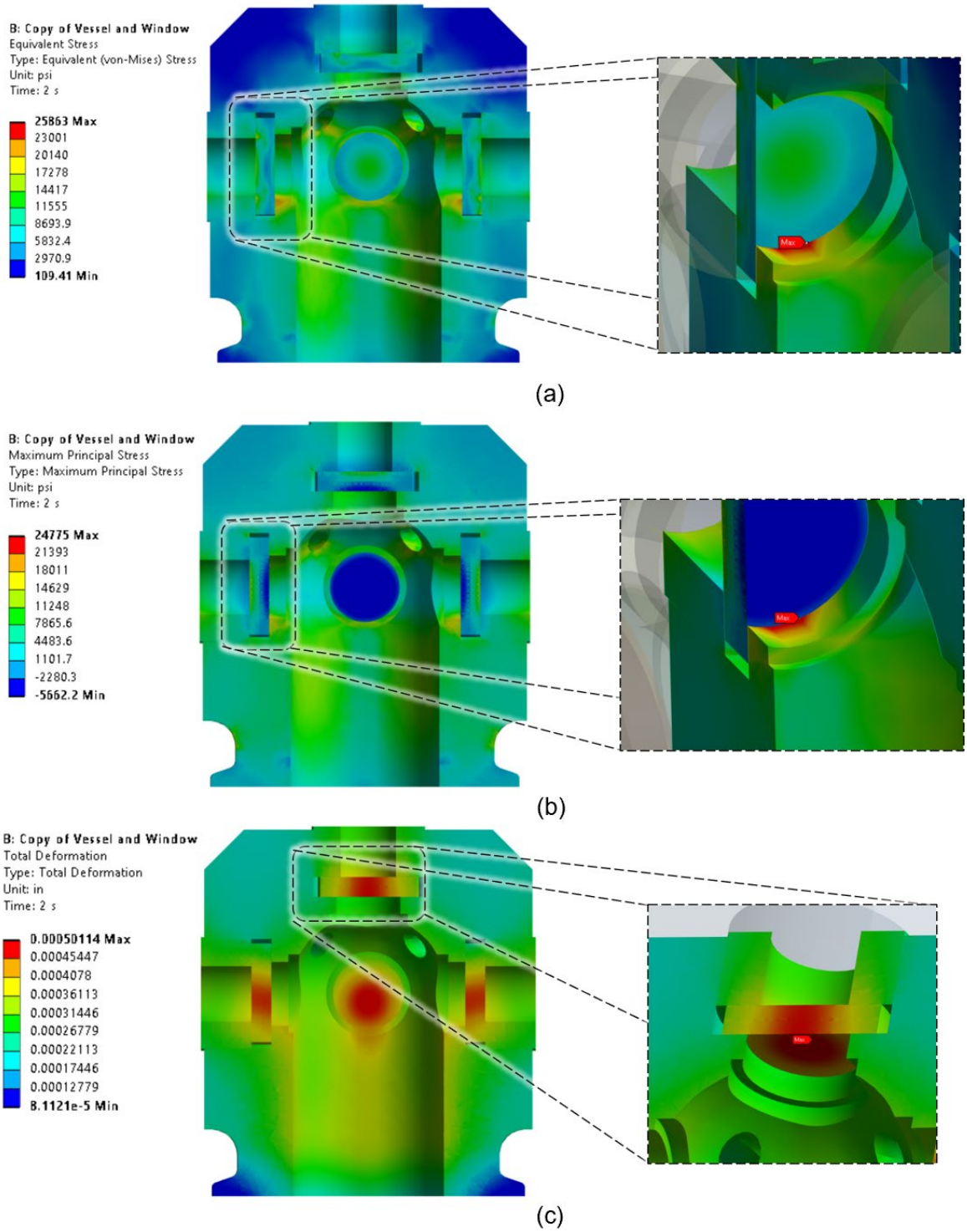

Figure 3.6: 3D pressure vessel model results, (a) and (b) show equivalent and 1st principal stress with the max stresses of 25.8 and 24.7 ksi, respectively, located at bottom of the window. (c) shows the max deflection (0.0005 inches) on the inside face of the windows

3.4.2 3D Pressure Vessel Wedge Model

The 3D pressure vessel wedge model and boundary conditions are shown in **Figures 3.7** and **3.8** respectively. This higher fidelity model focuses on quantifying displacements under load while leveraging the benefits of symmetry. This model includes additional interfaces, such as the pressure vessel cap and v-band clamp, and uses non-linear contacts (sliding and friction) to analyze the behavior of the pressure vessel under specific loading conditions.

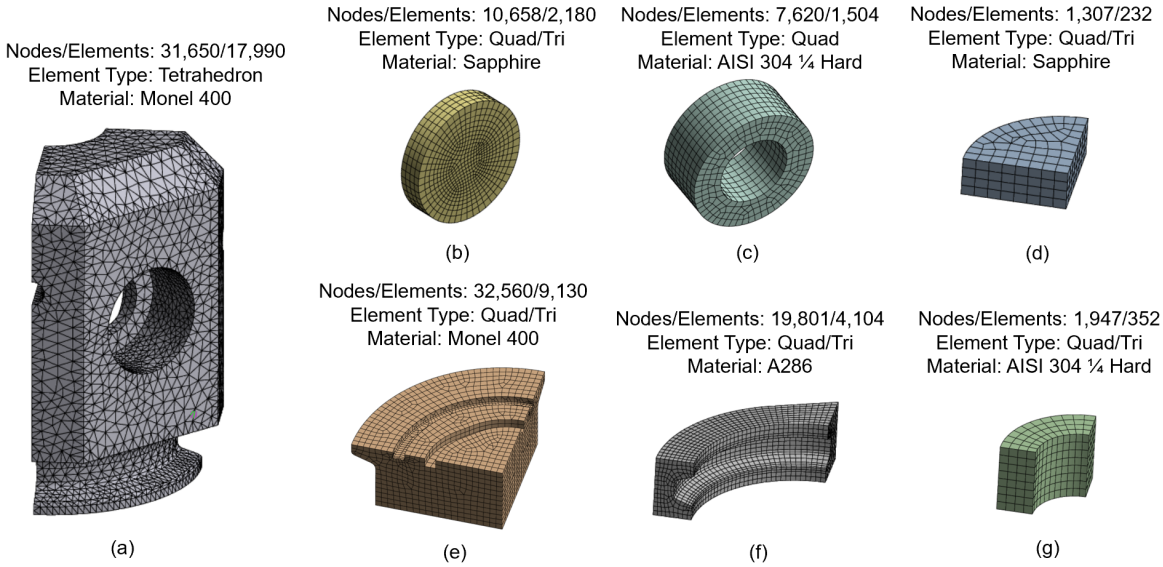

Figure 3.7: 3D Pressure vessel model wedge mesh details of the (a) pressure vessel body (b) & (d) windows, (c) & (g) window retention screws, (e) pressure vessel cap, and (f) v-band clamp

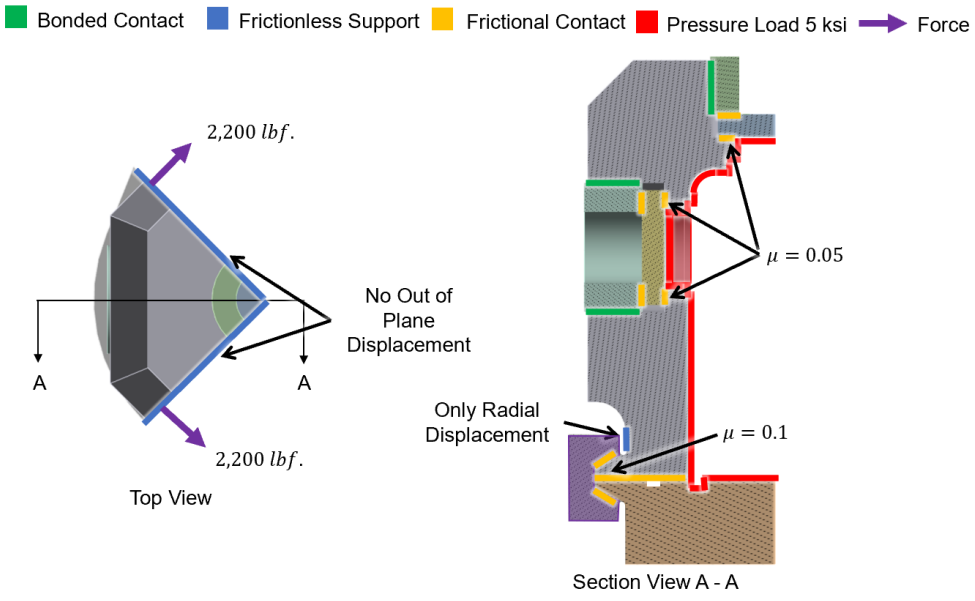

Figure 3.8: View of 3D pressure vessel wedge model boundary conditions

Figure 3.9 shows the FEA results, revealing that the highest stress occurs in the clamp, while the maximum displacement is observed at the cap. The peak displacement of the cap is at the centerline. The cap utilizes an O-ring for chamber sealing, which relies on maintaining compressive squeeze throughout operation. Deflections of the cap relative to the sealing surface on the pressure vessel were quantified as 0.0019 inches. Accounting for manufacturing tolerances [10], this leads to a 2.5% loss of squeeze when the chamber is subjected to proof pressures of 5 ksi. In summary, the o-ring is capable of sustaining a seal at twice the MWP.

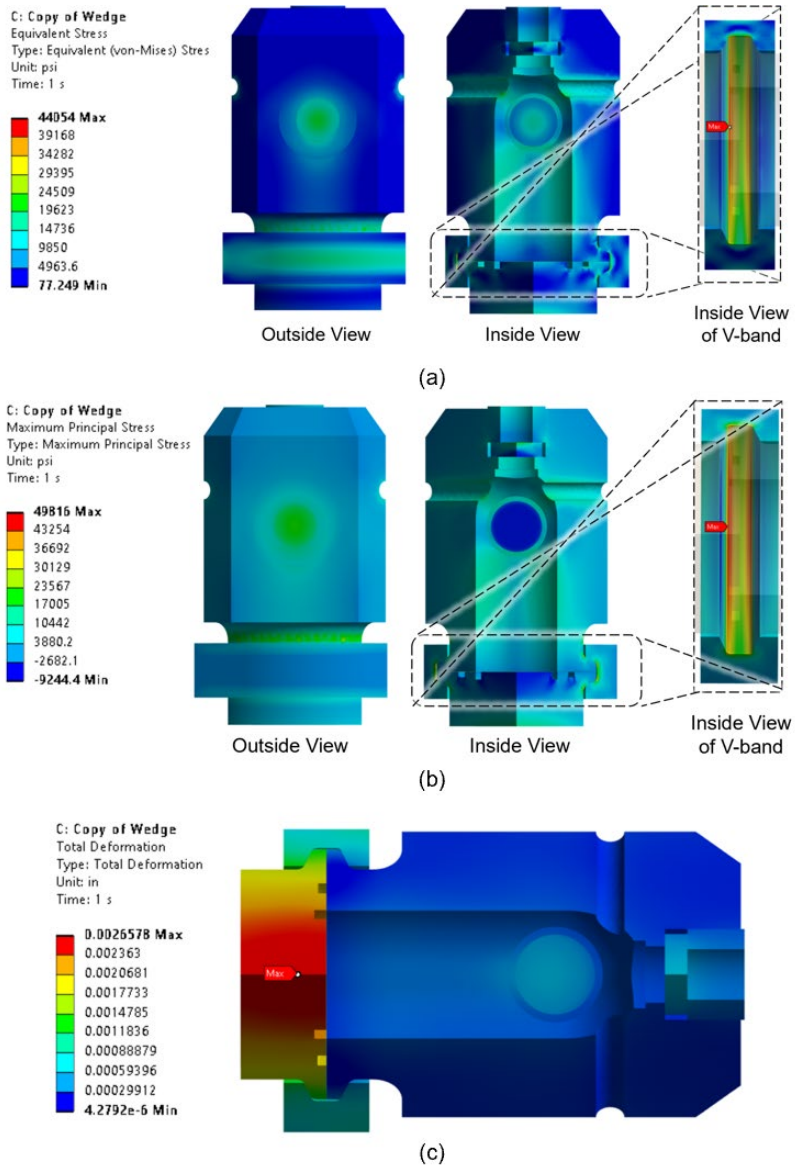

Figure 3.9: 3D pressure vessel wedge model results, (a) and (b) show equivalent and 1st principal stress with the max stresses of 44.1 and 49.8 ksi, respectively, located on the v-band clamp. (c) shows the max deflection (0.0027 inches) at the cap centerline.

3.4.3 3D Clamp Assembly Model

The 3D clamp assembly model and associated boundary conditions are shown in **Figures 3.10** and **3.11**, respectively. This higher fidelity sub model focuses on quantifying displacements under load while leveraging the benefits of symmetry. This model includes the additional components (bolt/nut spacer, links, and pin) to model the entire clamp half assembly. The model includes all the interfaces, between these components as non-linear contacts (sliding and friction) to analyze the behavior of clamp assembly under specific loading conditions.

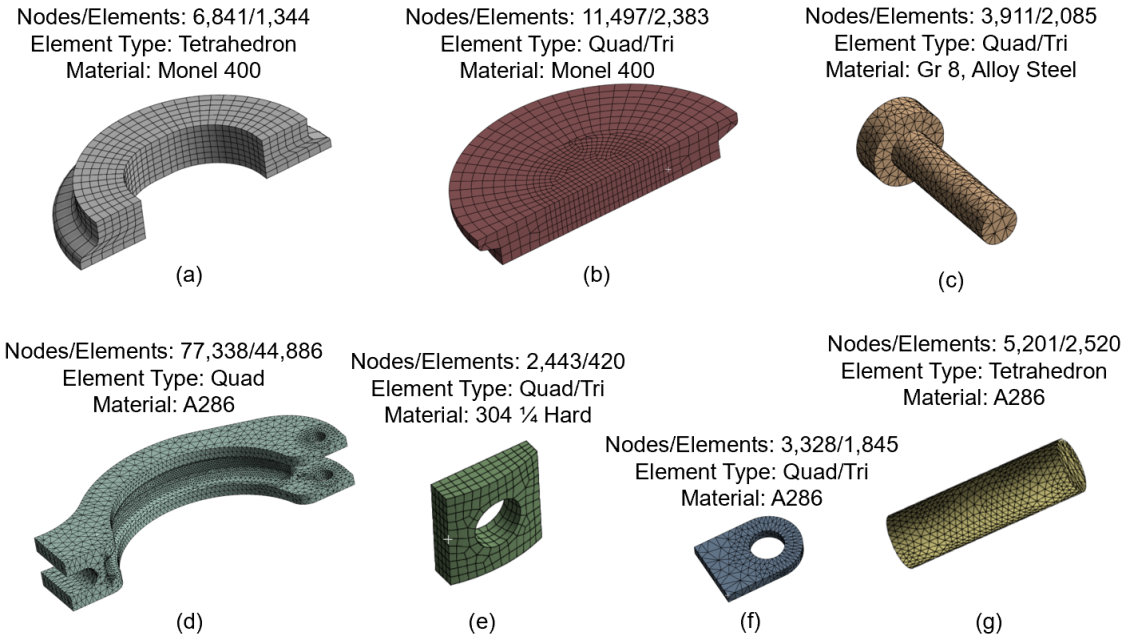

Figure 3.10: 3D clamp assembly model mesh details of the (a) pressure vessel body (b) the pressure vessel cap, (c) bolt & nut (d) v-band clamp half (e) spacer, (f) link and (g) pin

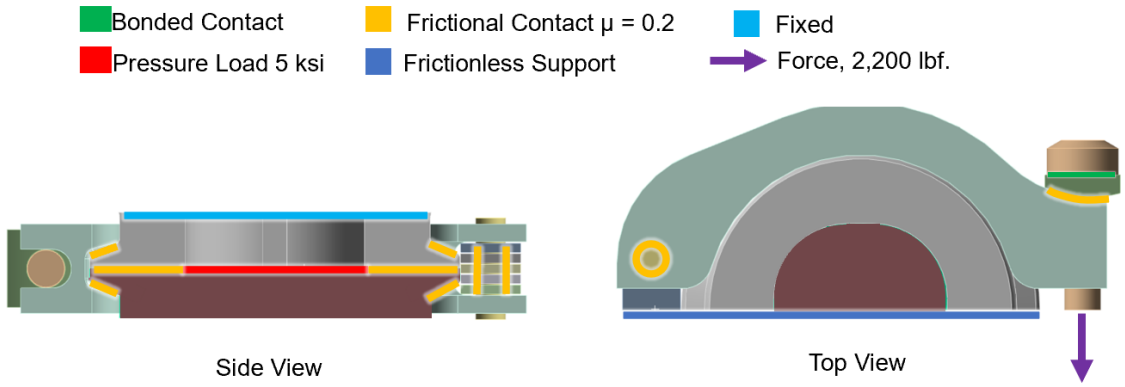

Figure 3.11: View of 3D clamp assembly model boundary conditions

FEA results, summarized in **Figure 3.12**, show that the peak stress is in the v-band clamp and the maximum displacement is near the bolt/nut. The peak stress on the v-band clamp has doubled and shifted away from the middle region toward the end compared to the wedge model (**sub-section 3.4.2)**, and is 8% of the yield strength of A286. The stress increase is due to two factors: stiffness and edge of contact stresses (EOC). Reduced self-supporting capability at the clamp ends decreases stiffness, resulting in higher local bending stress. EOC stress arises from frictional elastic contacts where the loaded body's edge opposes motion, causing increased shear at that location[17].

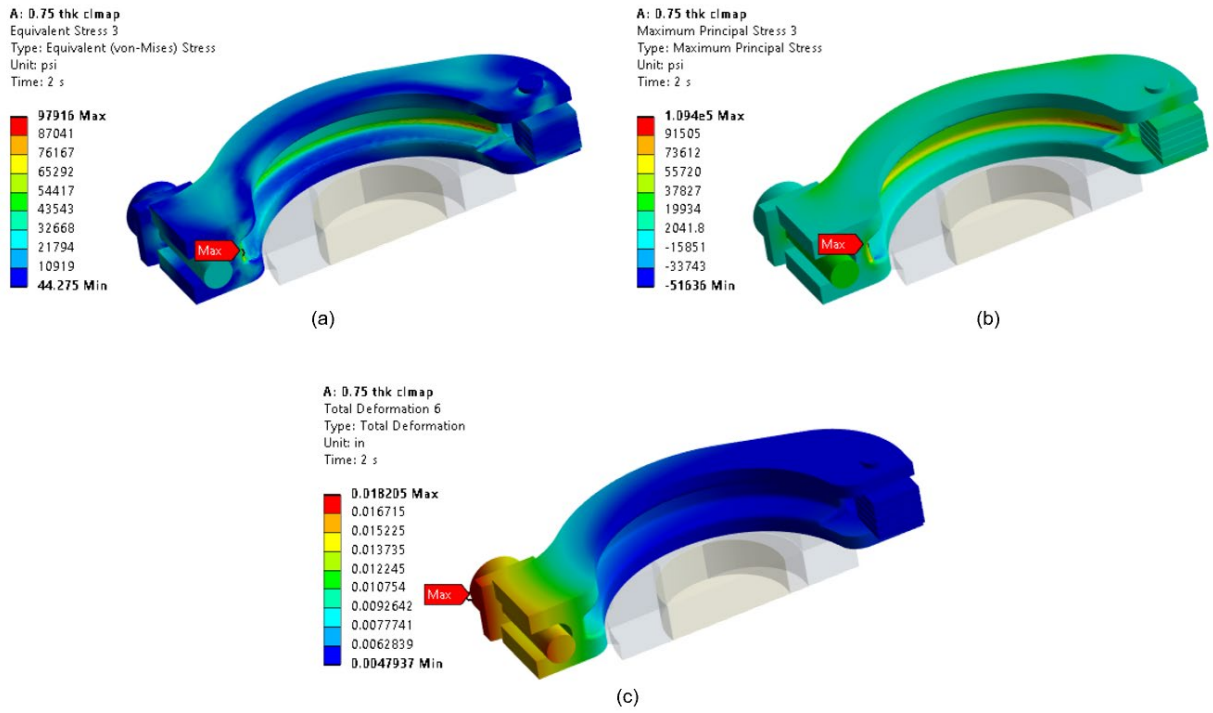

Figure 3.12: 3D clamp assembly model results, (a) and (b) show equivalent and 1st principal stress with the max stresses of 97.9and 109 ksi, respectively, located on the inside v-band clamp. (c) shows the max deflection (0.018 inches) at the bolt/nut.

3.4.4 The 2D Axisymmetric Window Retention Screw Model

The 2D Axisymmetric Window Retention Screw Model with boundary conditions is shown in **Figure 3.13** has been specifically developed to investigate the stress distribution and key behavior of areas surrounding the portholes and window retention threads.

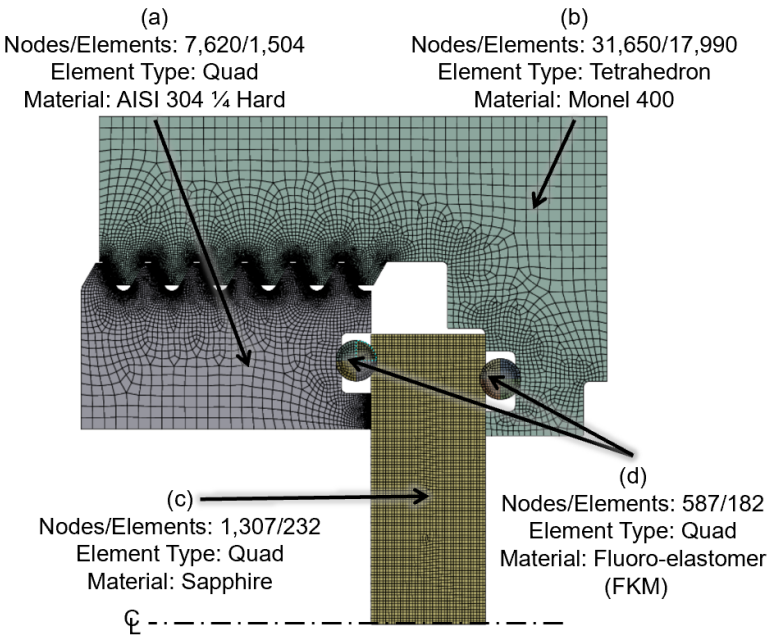

Figure 3.13: 2D Axisymmetric window retention screw model mesh details of the (a) window retention screw (b) the pressure vessel, (c) window, and (d) O-Rings

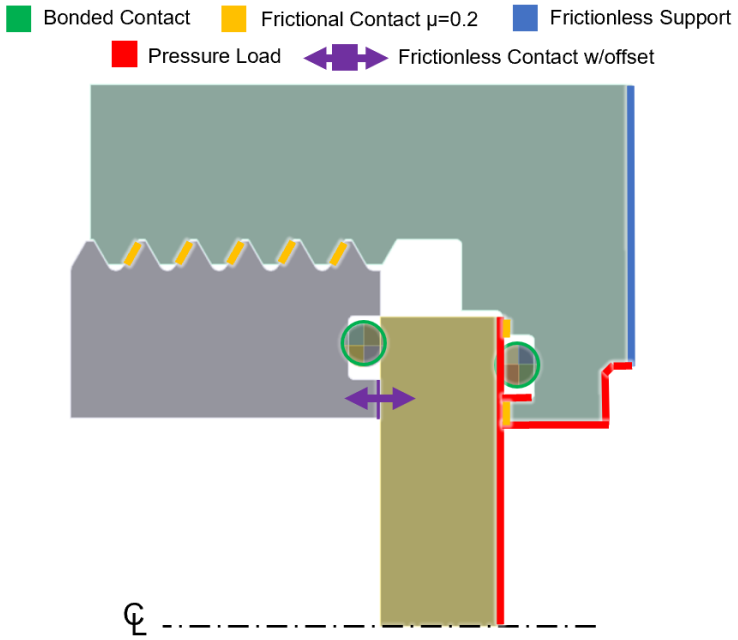

Figure 3.14: Boundary conditions of 2D axisymmetric window retention screw model

Figures 3.15 through **3.18** show the stress and displacement results for each key component, revealing important insights into the system behavior. Critically, the O-ring seal separation is negligible. The stress distribution in the bolt threads differs from the typical pattern where the lead

thread carries the highest load. In this case, the middle thread experiences the highest load due to the masking of the load path by the O-ring gland.

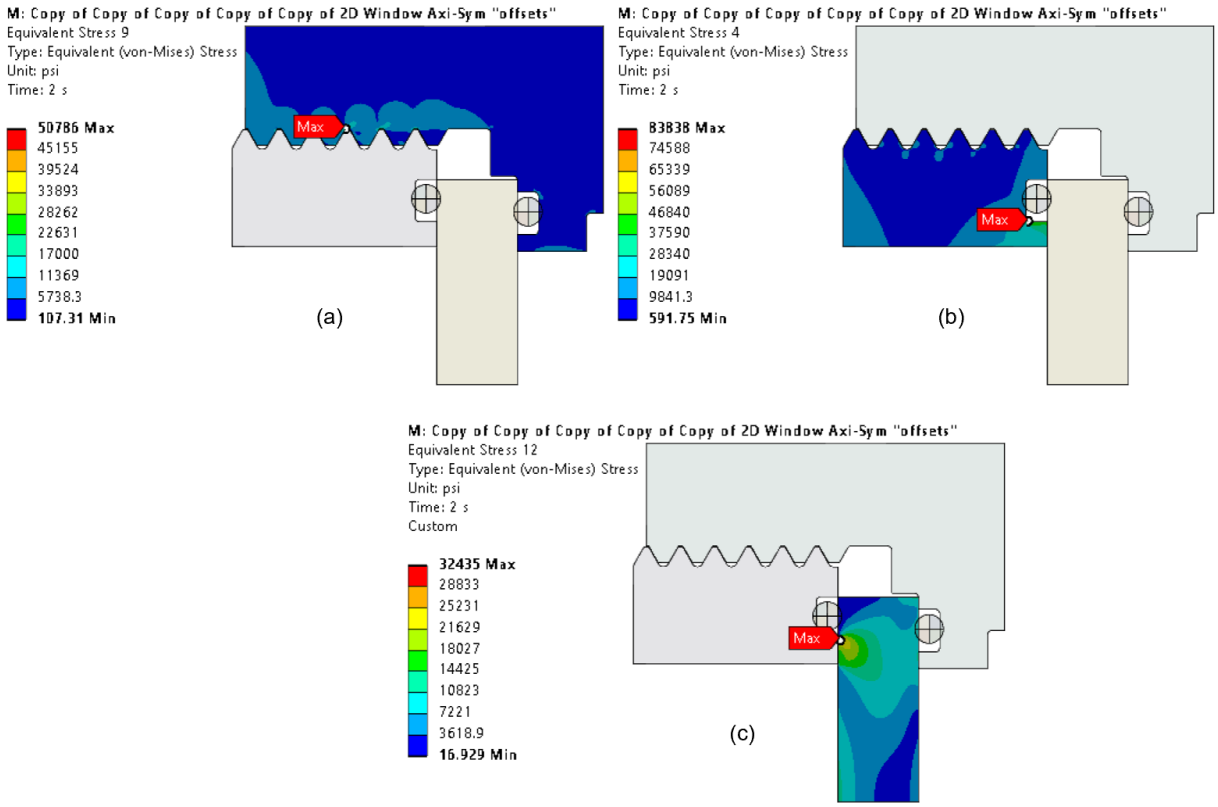

Figure 3.15: Equivalent stress results of 2D axisymmetric window retention screw model showing the (a) pressure vessel body max stress location is the 3rd thread root (b) window retaining screw max stress location is the gland corner and, (c) window max stress location at the contact region with the screw

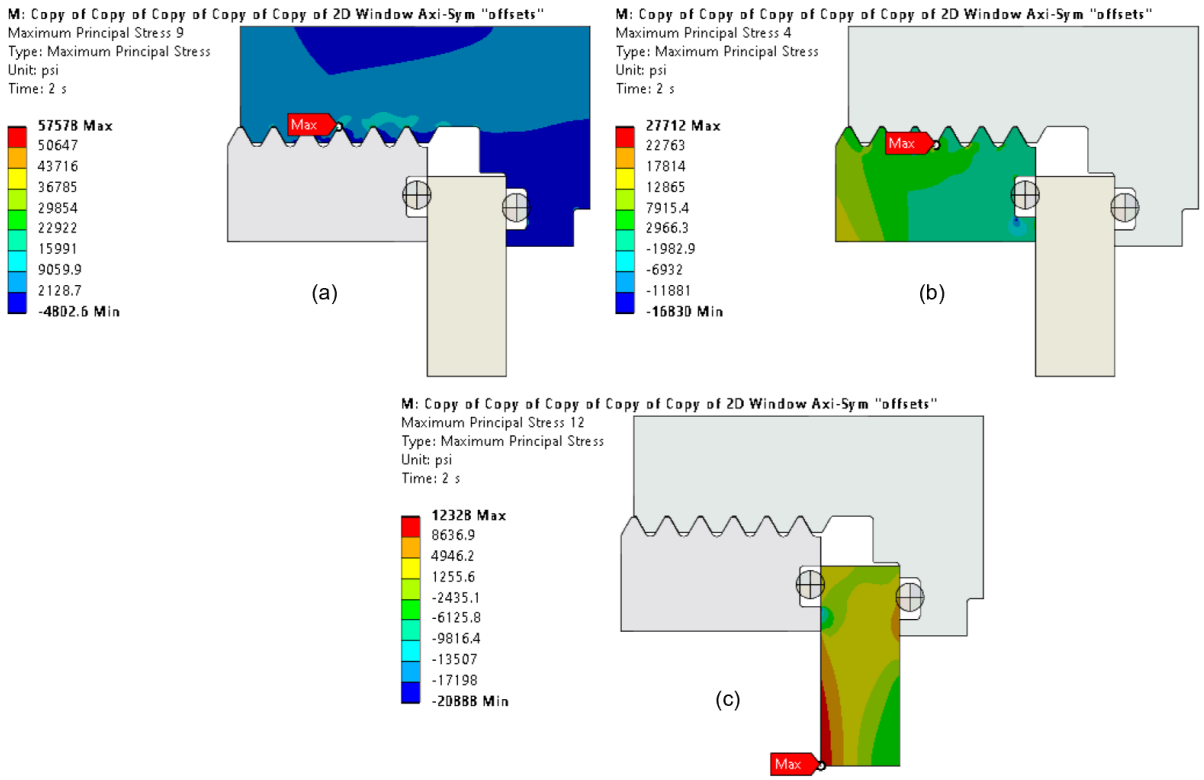

Figure 3.16: 1st principal stress results of 2D axisymmetric window retention screw model showing the (a) pressure vessel body max stress location is the 3rd thread root (b) window retaining screw max stress location is the 3rd thread root and, (c) window max stress location is centered on the outside face

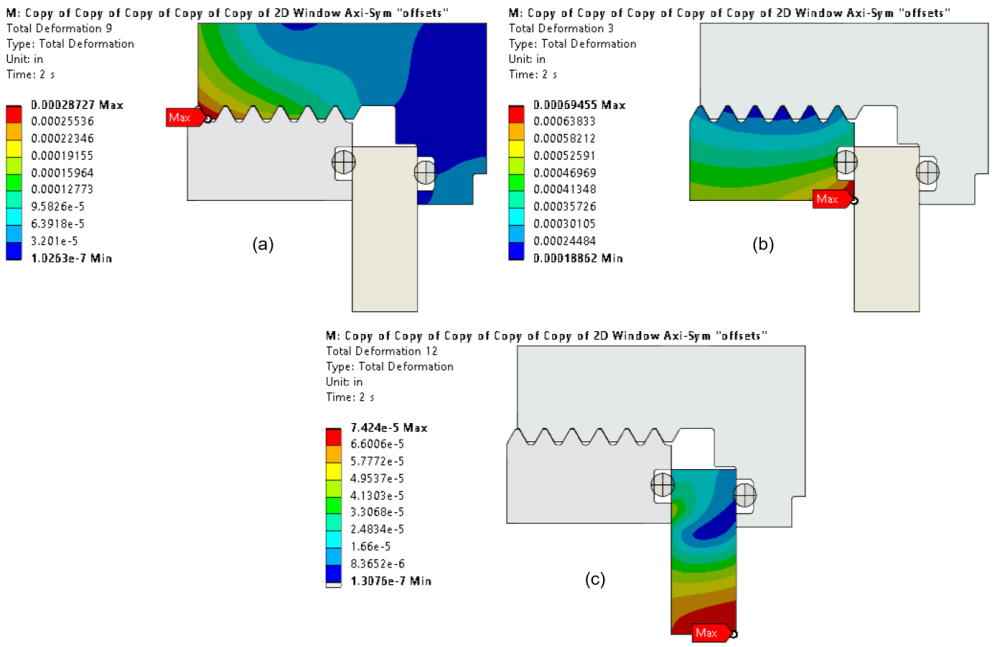

Figure 3.17: Total deformation results of 2D axisymmetric window retention screw model showing the (a) pressure vessel body max deflection location is the last thread (b) window retaining screw deflection location is window contact face and, (c) window max deflection location is centered on the inside face.

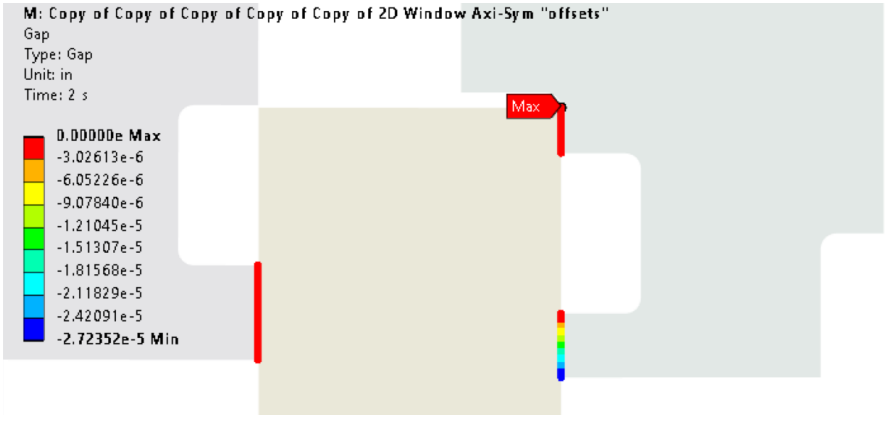

Figure 3.18: Contact separation results of 2D axisymmetric window retention screw model showing a gap opening of 27µinch.

3.5 Strength and Fatigue Assessments

Table 3-1 compares the results of the FEA analysis with the strength of the materials used in each component, showing the margin to both yield and tensile strength for each component. The majority of the components have >40% margin to yield strength. The two components with the

lowest strength margins are the clamp and bolt/nut and were assessed for potential fatigue life and durability of the system under a zero-max-zero load cycle. The results of the life analysis show that all the components have essentially infinite life, with at least 10^5 cycles to failure under worst case operating conditions.

Table 3-1: Component strength results

Component	**Material**	**Yield Strength (0.2%)** **Tensile Strength (Ultimate)** At room temp	**Peak Stress** Max Principal	**Margin**
Pressure Vessel	MONEL™ 400, hard	101.0 ksi 110.1 ksi	57.6 ksi	43.4 ksi (43%) 52.5 ksi (48%)
Vessel Cap	MONEL™ 400, hard	101.0 ksi 110.1 ksi	44.1 ksi	56.9 ksi (57%) 66.0 ksi (60%)
Window	Sapphire (99.9%)	85 ksi* *Modulus of rupture	12.23 ksi	72.8 ksi (86%)
Clamp Assy Half	A-286 Solution treated & aged	115.01 ksi 140.0 ksi	109.4 ksi	5.6 ksi (4.9%) 30.6 ksi (22%)
Clamp Bolt and Nut	Alloy Steel Gr 9	38.0 ksi 72.0 ksi	29.8 ksi	8.2 ksi (22%) 42.2 ksi (59%)
Spacer	AISI 304 SS ¼- Hardened	75.0 ksi 125.0 ksi	29.7 ksi	45.3 ksi (60%) 95.3 ksi (76%)
Window Retention Screw	AISI 304 SS ¼- Hardened	75.0 ksi 125.0 ksi	27.7 ksi	47.3 ksi (63%) 97.3 ksi (78%)

3.6 Rapid Adiabatic Compression

The rapid pressurization of gaseous oxygen presents a potential safety hazard due to the heat generated through adiabatic compression. Design guidance leveraged from [5] and [6], including strategies for designing high-pressure oxygen systems using distance volume pieces (DVPs) is shown in **Figure 3.19.**

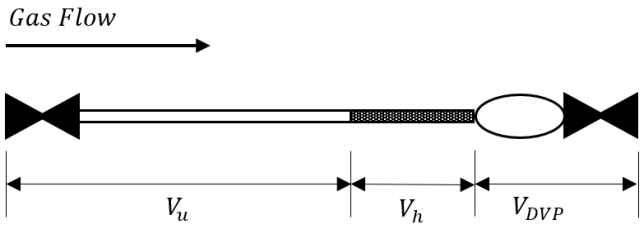

Figure 3.19: Diagram of distance volume piece arrangement (Adapted from [6])

To determine the minimum DVP volume (V_{DVP}) required for given upstream volume (V_u), hose volume (V_h), final/initial pressure ratio $\left(\frac{P_f}{P_i}\right)$ and safety factor (*SF*) parameters, the isentropic equation of state is

$$V_{DVP} = SF\,\frac{V_u + V_h}{\left(\frac{P_f}{P_i}\right)^{\frac{1}{\gamma}} - SF}, \tag{16}$$

where $\gamma = 1.4$ and minimum SF=1.2 [5]. The initial pressure (P_i) used is standard day sea-level pressure of $14.7\ psia$ at a room temperature of 70°F. The final pressure (P_f) used is the maximum pressure from a gas bottle, $2655\ psia$ [12]. All tube segments and fittings were assumed to be standard No4 size which results in a volume per unit length of 0.0296 in². Hose inner diameters segments were assumed to be standard ¼ inches which results in a volume per unit length of 0.0491 in². The upstream volume (V_u) includes all valves, tubing segments, and fittings up to the flex hose section (V_h) start, assumed to be 16 ft. in length. The volume hose segment V_h is assumed to be 18 inches.

To estimate the adiabatic temperature of the rapidly compressed slug of oxygen certain geometric and pressure conditions needs to be understood. The volume of the hot slug is

$$V_f = V_i\left(\frac{P_f}{P_i}\right)^{\frac{-1}{1-\gamma}}, \tag{17}$$

and is then needed for the calculation of the theoretical maximum temperature

$$T_f = T_i\left(\frac{V_i}{V_f}\right)^{\gamma-1}, \tag{18}$$

of the compressed slug. The results of the adiabatic compression analysis determined the minimum volume of the DVP to be 0.1984 in³. The as designed volume of the DVP is 0.258 in³ which increases the safety factor 29% to 1.55. The max temperature is 1878°F which assumes a 16ft section from the tank to the pressure supply valve. Rapid pressurization is defined as an increase in pressure that occurs in less than 50 m/s. To ensure the user safety, the HiPO pressurization and vent system uses multi-turn valves (slow opening valves and regulators) to prevent rapid pressurization to mitigate this effect.

CHAPTER 4: Observations of Particle Impact Ignition

4.1 Prototyping

A prototype of the HiPO LIPIT, shown in **Figures 4.1** and **4.2,** was fabricated and used to establish optimal optical alignment and end-user understanding. The prototype HiPO pressure vessel is a metal-coated, 3D-printed plastic vessel, engineered to withstand pressures up to 50 psi.

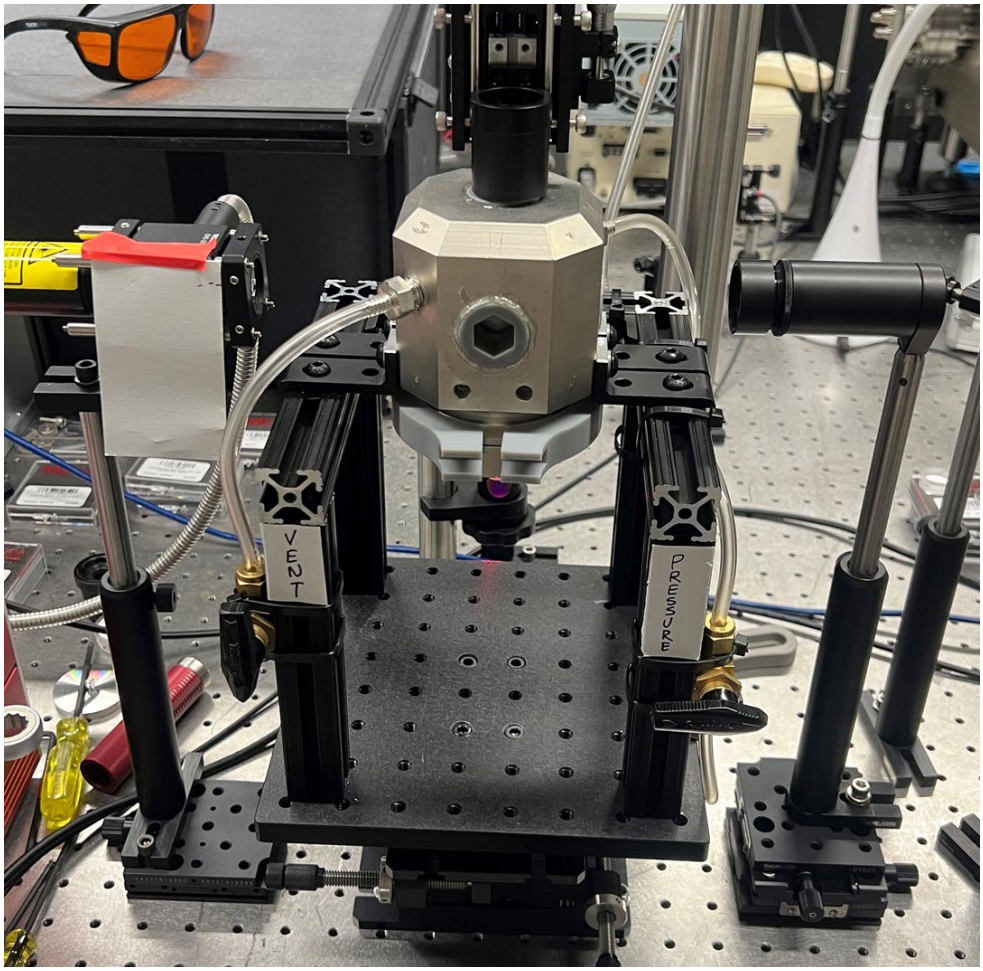

Figure 4.1: HiPO LIPIT prototype at the ISN

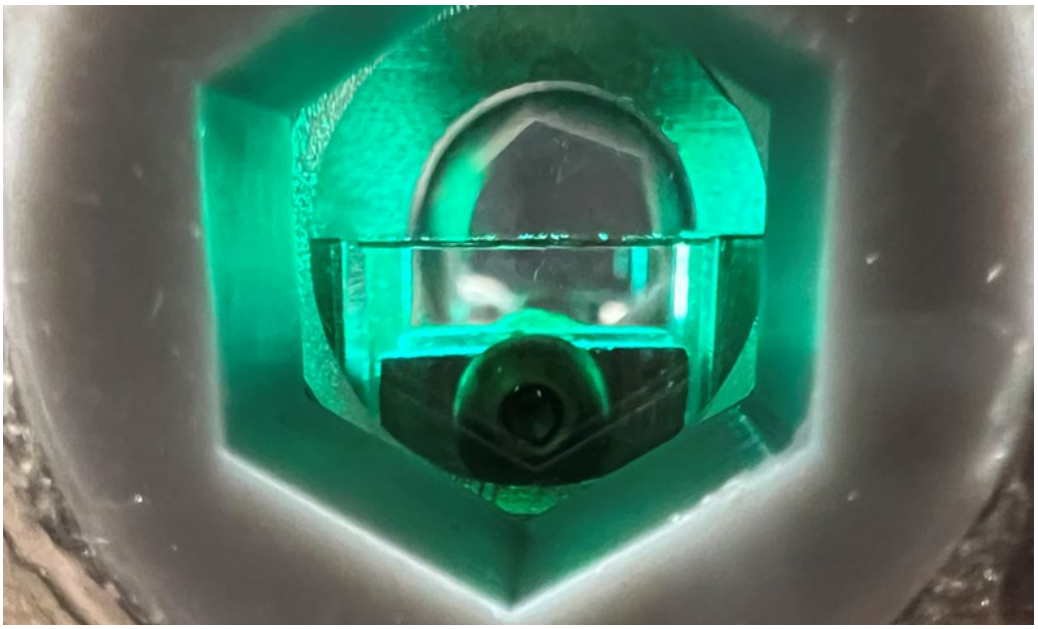

Figure 4.2: Test chamber view of the prototype HiPO LIPIT

4.2 Pathfinding Particle Ignition Experiments

To validate the design, a series of pathfinding particle impact experiments were performed using the prototype pressure vessel. Aluminum alloy (Al6061) and titanium alloy (Ti-6Al-4V) particles, with sizes ranging from 25 to 30 microns, were launched at a sapphire target. The pure O_2 atmosphere was established by purging the vessel with a continuous flow of oxygen gas at approximately 5 psi for a duration of one minute. Subsequently, the vent valve was sealed, and the oxygen pressure was increased to 25 psi.

A series of initial shots were executed with varying laser power settings to confirm precise laser focus, align the optics, and calibrate the relationship between laser power and particle velocity. **Figure 4.3** shows Al6061 and Ti-6Al-4V particles with impact velocities of 340 m/s and 120 m/s, respectively. The launch pad is on the left of the frame; the target is towards the right. The particles move from left to right during the experiment. Laser power within the range of 5-20 mW resulted in particle velocities in the ranges 100-700 m/s for Al6061 and 85-400 m/s for Ti-6Al-4V. These velocity ranges are sufficient to drive particle ignition, based on findings from past particle ignition experiments [5].

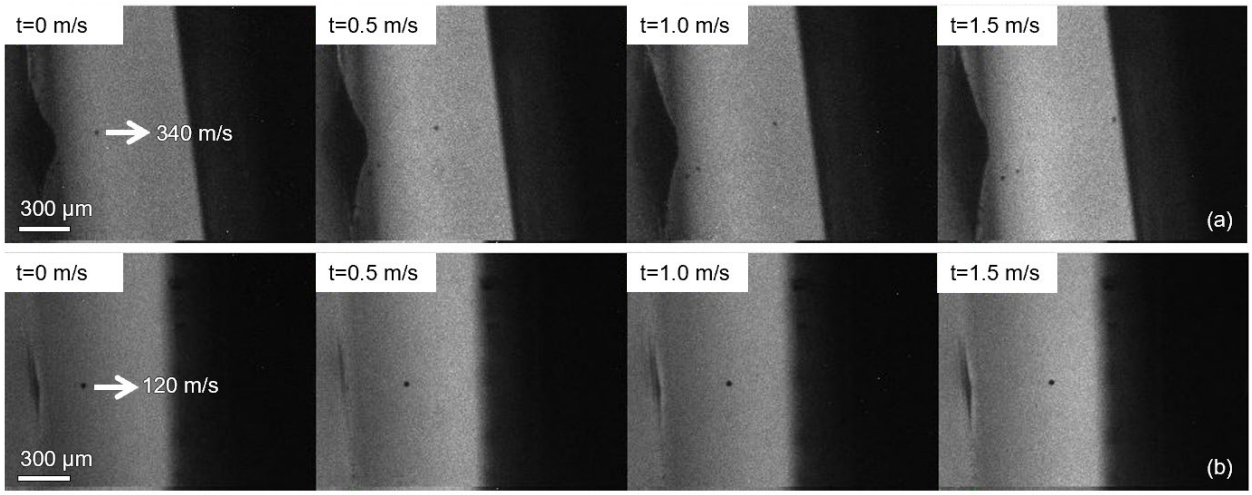

Figure 4.3: Trial LIPIT shot images using the HiPO LIPIT prototype with a 13 n/s exposure time using an Al6064 particle (a) traveling at 340 m/s and a Ti-6Al-4V particle (b) at 120 m/s

To capture particle ignition, we turned off the light source, increased the gain on the high-speed camera, and increased the camera exposure time such that any visible light emitted from particle ignition and burn would be detected by the camera. One frame from a reference shot with this dark configuration is shown in **Figure 4.4**. Note that in this reference shot, there is no particle launch. On the left of the frame, we see plasma left over from the laser ablation of the launchpad.

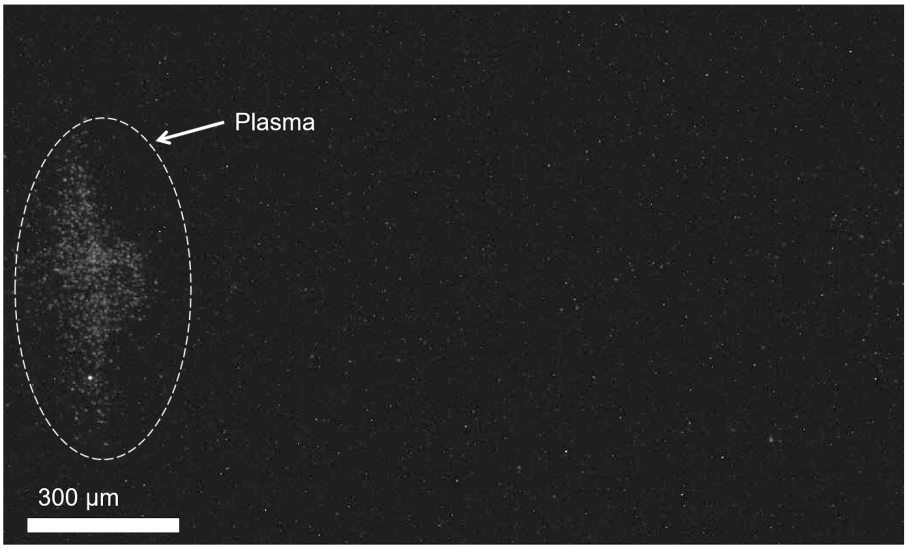

Figure 4.4: Reference shot in dark configuration showing ablative plasma and a 400 n/s exposure time

Employing the dark configuration, we made notable observations regarding Al6061 and Ti-6Al-4V particle ignition. Al6061 particles exhibited ignition at velocities of approximately 550 m/s

and 400 m/s. It is important to note that in this configuration, direct particle velocity tracking was not possible. Therefore, we estimated particle velocity using the previously recorded laser power-particle velocity relationship established during the setup process. Images of the particle ignition events shown in **Figure 4.5**. To establish that the emitted light originated from particle combustion, we superimposed the target surface demonstrating that the light emission occurred precisely at the target surface upon impact. In both cases, the ignition was visible within a single frame, lasting between 400 ns and 500 ns. The fact that the emission was solely observed at the target surface and the short duration of the light emission suggest that the intense straining and adiabatic heating were adequate for igniting Al6061 particles. However, at room temperature and under low oxygen pressure, the ignition of Al6061 particles was swiftly extinguished, and sustained burning did not occur. It is important to mention that among numerous shots, these were the only two instances of Al6061 particle ignition observed.

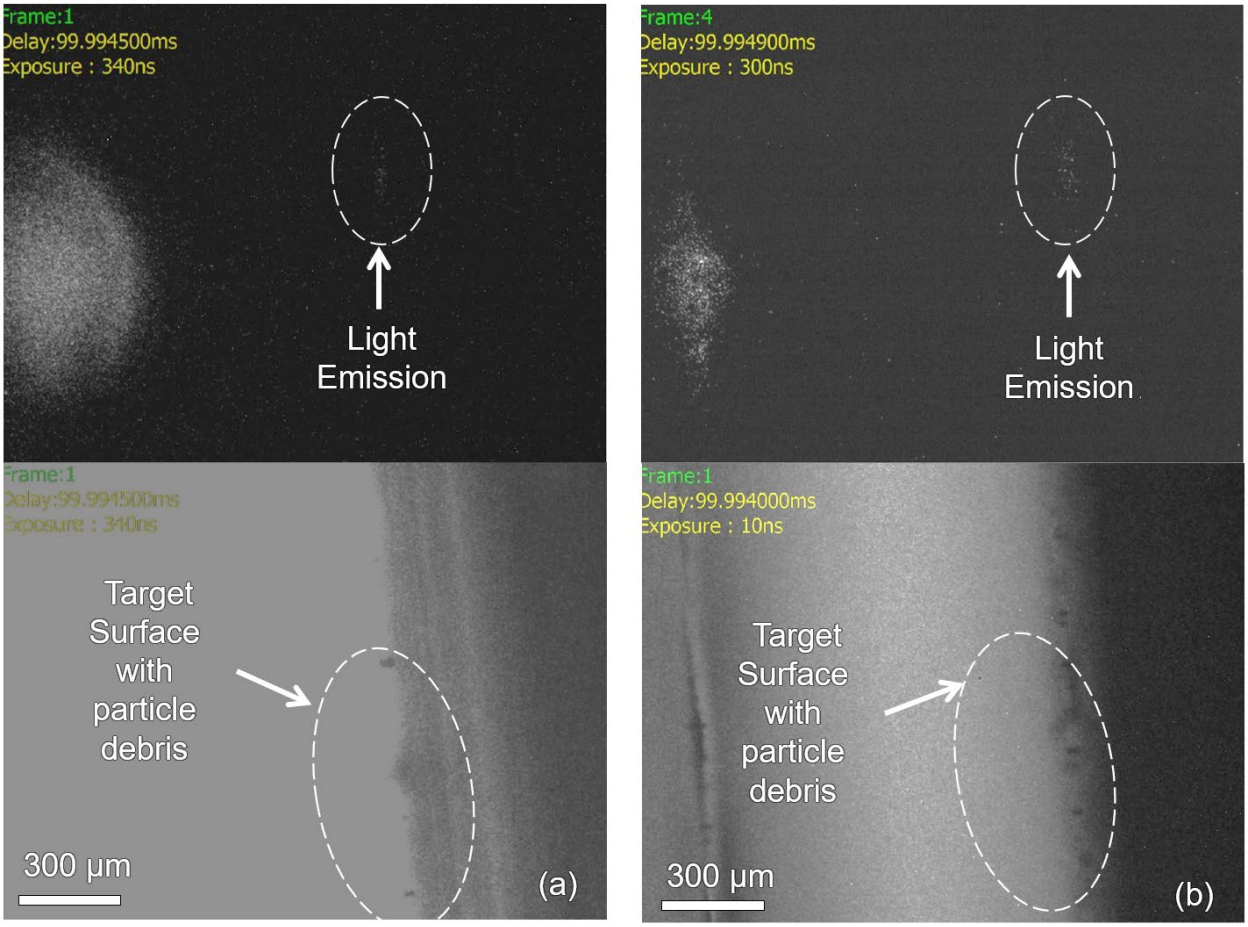

Figure 4.5: The images show Al6061 particle ignition with approx. velocities of (a) 550 m/s and (b) 400 m/s. The top image captured in the dark configuration and the lower image taken with a light source to highlight the target surface location within the frame.

In contrast, Ti-6Al-4V particles ignited much more readily than Al6061 and exhibited sustained burning. An illustrative example of Ti-6Al-4V ignition and continuous burning, with a particle impact velocity of approximately 250 m/s, is depicted in the image sequence presented in **Figure 4.6**. The ignition occurs upon impact with the sapphire target, and the particle continues to burn for approximately 3.2 µs. It is worth noting that in this sequence, the particle has rebounded from the target and is moving towards the left, while the reflected image of the target surface is visible on the right side of the frame.

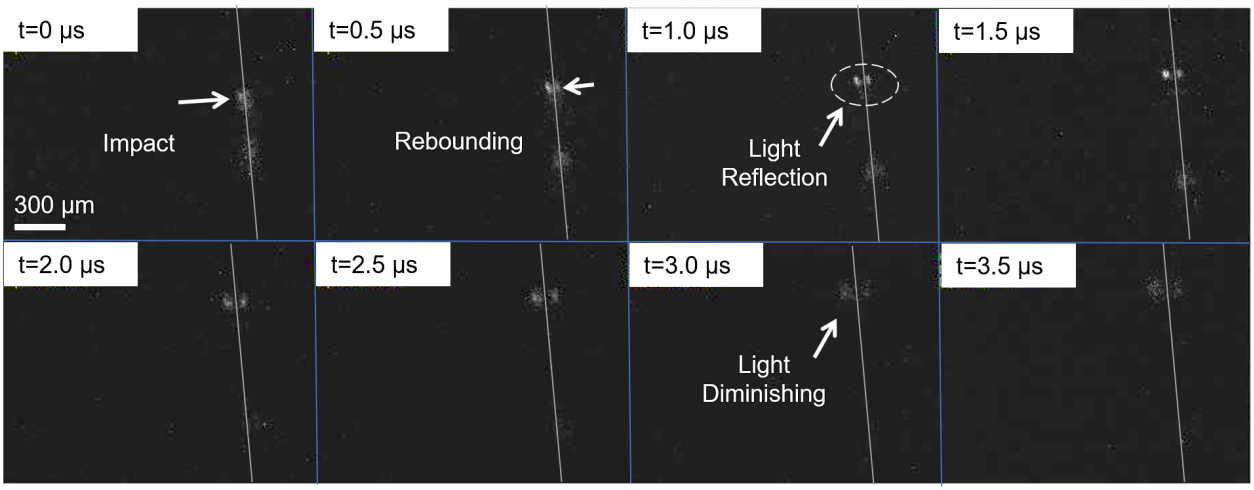

Figure 4.6: Ti-6Al-4V particle impact ignition, rebounding, and light emission from burning with target surface overlaid

Among the observed ignition events, particle fragmentation upon impact and sustained burning of the fragments were frequently noted, as shown in **Figure 4.7**. The fragments exhibited rapid velocities, possibly due to jetting upon impact. In several other cases, the emitted light from the particle gradually diminished, as illustrated in **Figure 4.8**. Several explanations could account for the cessation of light emission: the particle may have been nearly fully consumed during burning, the particle burn may have been close to extinguishment, or, most likely, the particle rebounded out of the plane of focus. Nevertheless, Ti-6Al-4V particle burn was observed for several microseconds, indicating that adiabatic strain heating and resulting oxidation reactions were sufficient to ignite the particles and sustain combustion at room temperature under low oxygen pressure.

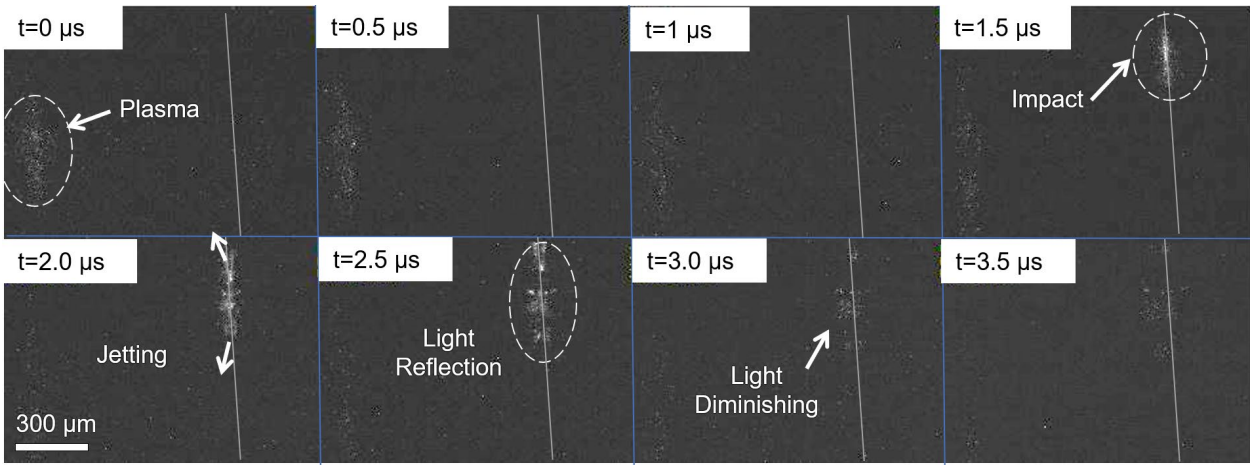

Figure 4.7: Ti-6Al-4V particle impact fragmentation and jetting with target surface overlaid

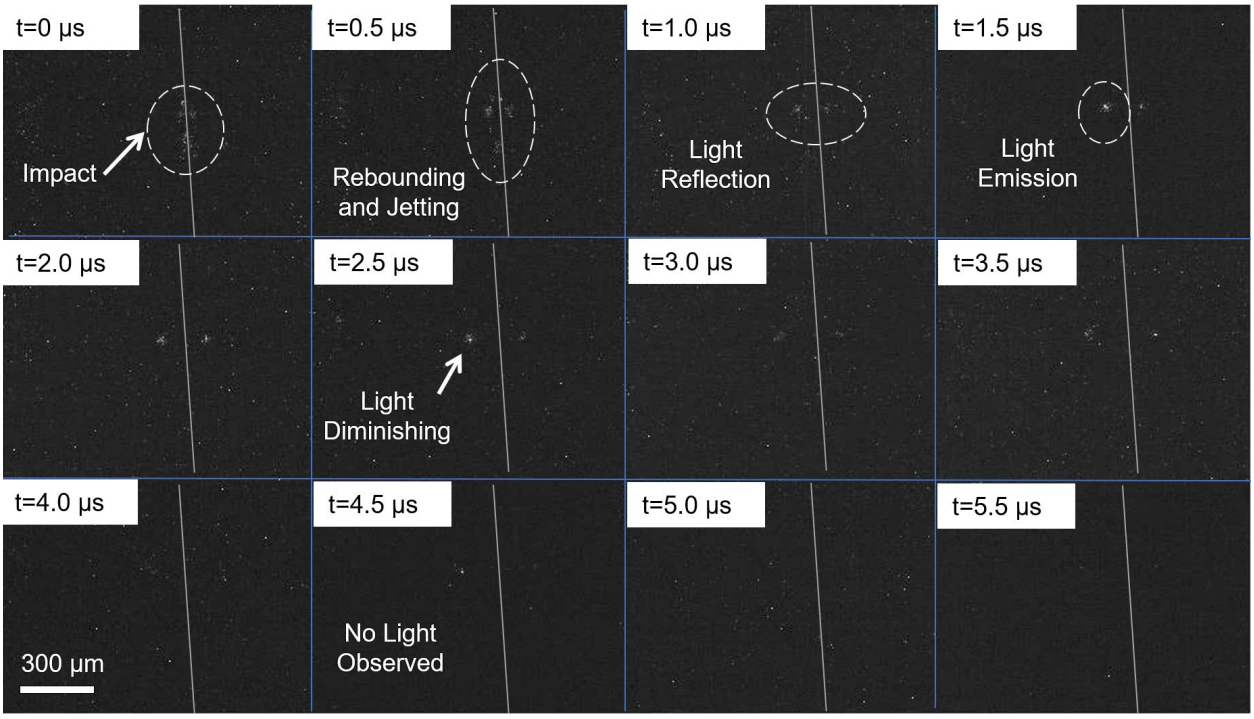

Figure 4.8: Ti-6Al-4V particle impact showing diminishing light emission after impact & target surface overlaid

Given that Ti-6Al-4V particles ignited and burned readily, we gauged the probability of ignition as a function of particle velocity range, as shown in **Table 4-1** below. For a given laser power, we determined the average particle velocity by measuring particle velocity over 10 shots. We then performed several shots with the dark configuration and recorded the frequency of particle ignition events at that given laser power. With this brief analysis, we determine that in these test conditions, the critical velocity for Ti-6Al-4V particle ignition is in the range 200-225 m/s.

Table 4-1: Summary of Ti-6Al-4V particle ignition events

Laser Power (mW)	Average Velocity (m/s)	Ignition Events
16	253.8±47	13/15
15.3	250.2±52	3/6
12.9	172.4±45	3/22
10.1	148±43	0/10
7.6	141±23	0/10
5.1	115±32	0/6

CHAPTER 5: Conclusions

This thesis is a comprehensive evaluation of the HiPO LIPIT system and provides insights into its structural integrity and operational capabilities. The results obtained from various analyses, including sizing assessments, stress calculations, FEA modeling, rapid adiabatic compression analysis, and strength/fatigue assessment, contribute to a thorough understanding of the system performance and response under different load cases and worst-case scenarios. To validate the design, HiPO LIPIT experiments were successfully conducted using a prototype pressure vessel. These pathfinding experiments successfully demonstrated in situ imaging of ignition of Al6061 and Ti-6Al-4V particles.

5.1 HiPO LIPIT Key Results

The analyses outlined in **Chapter 3** show that the HiPO LIPIT system was designed with high level of safety and conservative assessment. **Table 5-1** summarizes design compliance.

Table 5-1: Summary of requirement compliance

Component	Requirement (Source)	Results	Status
HiPO LIPIT System	MWP of 2.50 ksi **(Section 2.1)**	System capable of 5 ksi	Exceeds
HiPO LIPIT System	O_2 compatible materials **(Section 2.1)**	All materials recommended by ASTM Manual 36 [5]	Meets
HiPO LIPIT System	Integrates with LIPIT **(Section 2.1)**	Testing with Prototype has been successful	Meets
HiPO LIPIT System	Follows Industry Standards **(Section 2.1)**	*Described below*	-
Pressure Vessel	All stresses <16.7 ksi [7]	Max stress of 12.5 ksi	Exceeds
O-rings	Min Seal squeeze 19% [10]	Limiting O-ring (cap) at 19.5% at MWP	Exceeds
Window	Min. SF=4 [14]	As Designed Safety Factor 5.81	Exceeds
DVP	Min. SF=1.2 [6]	As Designed Safety Factor 1.55	Exceeds

The experimental tests conducted on the prototype pressure vessel validated the HiPO design and compatibility with the LIPIT system. Particle impact experiments were carried out using Al6061 and Ti-6Al-4V particles in a controlled environment of 25 psi O_2. Al6061 particles exhibited

ignition at velocities of approximately ~400 and 550 m/s. The intense straining and adiabatic heating induced by the impact were sufficient to ignite the particles; however, the ignition was rapidly extinguished at room temperature and relatively low oxygen pressure. Ti-6Al-4V particles, on the other hand, ignited more readily and showed sustained burning. An example sequence showed ignition and continuous burning for approximately 3.2 μs at a particle impact velocity of 250 m/s.

Fragmentation upon impact and sustained burning of the fragments were frequently observed during the ignition events. Additionally, the emitted light from the particles sometimes diminished, possibly due to particle consumption, near-extinguishment, or particle rebounding out of the plane of focus. The analysis of the probability of Ti-6Al-4V particle ignition revealed that the critical velocity fell within the range of 200-225 m/s under the given test conditions.

5.2 Future Work

The successful design allows for ongoing HiPO LIPIT experiments on the prototype vessel. Although currently limited to a chamber pressure of 50 psi, it can serve as a valuable tool for conducting particle impact and ignition testing for an extended period. Once the manufacturing of the Monel vessel is finished, HiPO LIPIT pressures can be increased to up to 2.5 ksi. This will enable researchers to investigate the effects of operating conditions and material choices on susceptibility to particle impact ignition with the ultimate goal to develop more durable oxygen-compatible hardware for next-generation staged combustion rocket engines.

Bibliography

[1] Veysset, D., Lee, J.-H., Hassani, M., Kooi, S. E., Thomas, E. L., and Nelson, K. A. "High-Velocity Micro-Projectile Impact Testing." *Applied Physics Reviews*, Vol. 8, No. 1, 2021, p. 011319. https://doi.org/10.1063/5.0040772.

[2] Imbriglio, S. I., Hassani-Gangaraj, M., Veysset, D., Aghasibeig, M., Gauvin, R., Nelson, K. A., Schuh, C. A., and Chromik, R. R. "Adhesion Strength of Titanium Particles to Alumina Substrates: A Combined Cold Spray and LIPIT Study." *Surface and Coatings Technology*, Vol. 361, 2019, pp. 403–412. https://doi.org/10.1016/j.surfcoat.2019.01.071.

[3] Chen, S. H., Souna, A. J., Soles, C. L., Stranick, S. J., and Chan, E. P. "Using Microprojectiles to Study the Ballistic Limit of Polymer Thin Films." *Soft Matter*, Vol. 16, No. 16, 2020, pp. 3886–3890. https://doi.org/10.1039/D0SM00295J.

[4] Cherston, J., Veysset, D., Sun, Y., Yano, H., Nelson, K. A., Murari, S., and Paradiso, J. A. Large-Area Electronic Skins in Space: Vision and Preflight Characterization for First Aerospace Piezoelectric e-Textile. Presented at the Sensors and Smart Structures Technologies for Civil, Mechanical, and Aerospace Systems, Online Only, United States, 2020.

[5] Beeson, H., Smith, S., and Stewart, W. *Safe Use of Oxygen and Oxygen Systems: Handbook for Design, Operation, and Maintenance: Second Edition*. ASTM International, 2007.

[6] Santay, A., Becker, I., and Werley, B. Design Strategies for Polymer-Lined Flex-Hose Distance/Volume Pieces. In *Flammability and Sensitivity of Materials in Oxygen-Enriched Atmospheres: Eighth Volume* (T. Chou, W. Royals, and T. Steinberg, eds.), ASTM International, 100 Barr Harbor Drive, PO Box C700, West Conshohocken, PA 19428-2959, 1997, pp. 93-93–15.

[7] ASME/BPVC SEC VIII-1 - SECTION VIII DIVISION 1 RULES FOR CONSTRUCTION OF PRESSURE VESSELS - Engineering Workbench. https://ewb.ihs.com. Accessed May 17, 2023.

[8] Ansys, Inc. 2023. Ansys GRANTA EduPack Software. Cambridge, UK: Ansys, Inc. Retrieved from Www.Ansys.Com/Materials. .

[9] Sapphire Windows. https://www.thorlabs.com. Accessed May 17, 2023.

[10] SAE International. 2021. SAE AS6235B - Face Seal Gland Design, Static, O-Ring and Other Seals for Aerospace Hydraulic and Pneumatic Applications - Includes Access to Additional Content - Engineering Workbench. https://ewb.ihs.com. Accessed May 17, 2023.

[11] SAE International. 2020. SAE AS1895E - Coupling Assembly, V-Retainer, High Pressure High Temperature, Pneumatic Tube - Engineering Workbench. https://ewb.ihs.com. Accessed May 17, 2023.

[12] U.S. Department of Transportation. (2017). 3AA2400 Seamless Steel Gas Cylinders. (DOT-SP 8162). .

[13] Pilkey, W. D., and Pilkey, D. F. *Peterson's Stress Concentration Factors*. John Wiley & Sons, Inc., Hoboken, NJ, USA, 2007.

[14] Specialist Data Sheets for Optical Materials. https://www.crystran.co.uk/documents. Accessed May 17, 2023.

[15] Bolt Torque Calculator. https://www.engineeringtoolbox.com/bolt-torque-load-calculator-d_2065.html. Accessed May 17, 2023.

[16] Smithells, C. J., Gale, W. F., and Totemeier, T. C. *Smithells Metals Reference Book*. Elsevier Butterworth-Heinemann, Amsterdam ; Boston, 2004.

[17] SACKFIELD, A., Hills, D. A., and Nowell, D. *Mechanics of Elastic Contacts*. Elsevier, 2013.